Bioactive Materials 8 (2022) 309–324

Contents lists available at ScienceDirect

Bioactive Materials

journal homepage: www.sciencedirect.com/journal/bioactive-materials

Rational integration of defense and repair synergy on PEEK osteoimplants via biomimetic peptide clicking strategy

Meng Li [a,d,1], Jiaxiang Bai [a,1], Huaqiang Tao [a,1], Li Hao [e], Weiling Yin [b], Xiaoxue Ren [c], Ang Gao [c], Ning Li [a], Miao Wang [b], Shiyuan Fang [d], Yaozeng Xu [a], Liang Chen [a], Huilin Yang [a], Huaiyu Wang [c,*], Guoqing Pan [b,**], Dechun Geng [a,***]

[a] Department of Orthopaedics, The First Affiliated Hospital of Soochow University, 188 Shizi Street, Suzhou, 215006, Jiangsu, China
[b] Institute for Advanced Materials, School of Materials Science and Engineering, Jiangsu University, 301 Xuefu Road, Zhenjiang, 212013, Jiangsu, China
[c] Center for Human Tissues and Organs Degeneration, Shenzhen Institutes of Advanced Technology, Chinese Academy of Sciences, Shenzhen, 518055, Guangdong, China
[d] Department of Orthopaedics, The First Affiliated Hospital of USTC, University of Science and Technology of China, 17 Lujiang Road, Hefei, 230001, Anhui, China
[e] Department of Oncology, The First Affiliated Hospital of USTC, University of Science and Technology of China, 17 Lujiang Road, Hefei, 230001, Anhui, China

ARTICLE INFO

Keywords:
Surface biomodification
Polyetheretherketone
Anti-infectivity and osteo-inductivity
Mussel adhesion
Bioorthogonal chemistry

ABSTRACT

Polyetheretherketone (PEEK) has been widely used as orthopedic and dental materials due to excellent mechanical and physicochemical tolerance. However, its biological inertness, poor osteoinduction, and weak antibacterial activity make the clinical applications in a dilemma. Inspired by the mussel adhesion mechanism, here we reported a biomimetic surface strategy for rational integration and optimization of anti-infectivity and osteo-inductivity onto PEEK surfaces using a mussel foot proteins (Mfps)-mimic peptide with clickable azido terminal. The peptide enables mussel-like adhesion on PEEK biomaterial surfaces, leaving azido groups for the further steps of biofunctionalizations. In this study, antimicrobial peptide (AMP) and osteogenic growth peptide (OGP) were bioorthogonally clicked on the azido-modified PEEK biomaterials to obtain a dual-effect of host defense and tissue repair. Since bioorthogonal clicking allows precise collocation between AMP and OGP through changing their feeding molar ratios, an optimal PEEK surface was finally obtained in this research, which could long-term inhibit bacterial growth, stabilize bone homeostasis and facilitate interfacial bone regeneration. In a word, this upgraded mussel surface strategy proposed in this study is promising for the surface bioengineering of inert medical implants, in particular, achieving rational integration of multiple biofunctions to match clinical requirements.

1. Introduction

Polyetheretherketone (PEEK) is a special kind of thermoplastic engineering plastic which has been widely used in orthopedics and maxillofacial surgery with regard to its excellent mechanical properties close to cortical bone and the extraordinary stability in physiological environments [1]. However, with the gradual improvement of medical standards, the conventional PEEK materials can not fulfill the high requirements of bone implantation, as they are bioinert and always confront with the problems of insufficient osseointegration and postoperative bacterial infection [2,3]. These two risks usually cause implant loosening, delayed healing, and even the failure of implantation, posing a tremendous burden on patients and the whole society [4,5]. Therefore, the orthopedic prostheses made of PEEK need further functionalizations to improve the peri-implant osteogenesis and anti-infective activity.

For the achievement of anti-infective functions, various antibacterial agents such as antibiotics, quaternary ammonium compounds (QACs), as well as some metals (i.e., Ag and Cu) and their oxides are commonly used to modify the surface of bone implants [6–8]. Nevertheless, all

Peer review under responsibility of KeAi Communications Co., Ltd.
* Corresponding author.
** Corresponding author.
*** Corresponding author.
E-mail addresses: hy.wang1@siat.ac.cn (H. Wang), panguoqing@ujs.edu.cn (G. Pan), szgengdc@163.com (D. Geng).
[1] These authors contributed equally to this work.

https://doi.org/10.1016/j.bioactmat.2021.07.002
Received 21 May 2021; Received in revised form 15 June 2021; Accepted 1 July 2021
Available online 10 July 2021

these functional components are concerned about their potential toxicity to human bodies, and the abuse of antibiotics may even aggravate the development of new multi-drug resistant bacteria (MDRB) [9–11]. Alternatively, antimicrobial peptides (AMPs) are an emerging kind of antibacterial agents, which are attactive for their biogenic nature and high efficiency [12]. With the functions different from other antibacterial agents, AMPs can target and concentrate on the cytoplasmic membranes of pathogens, dislocate the membrane proteins to hamper cell wall synthesis and cell respiration, and ultimately lead to the death of pathogen [13–15]. Therefore, AMPs are widely used for the anti-infective therapy with a relatively low-risk of causing bacterial drug-resistant mutations and cytotoxicity. Up to now, there are numerous studies about the surface functionalization of biomaterials with AMPs. Despite significant gains have been made, the single use of AMPs is far from perfect as the lack of osteogenic properties is another major concern for the PEEK implants as mentioned above. It is noteworthy that the bio-functions of peptides are diverse, and some other peptides such as osteogenic growth peptide (OGP) is well known for its osteogenic properties [16]. As an endogenous peptide presented in mammalian serum, OGP has been well studied in its free or tethered states to regulate the osteogenic differentiation of bone marrow mesenchymal stem cells and further promote matrix mineralization, thereby can be used to promote bone regeneration after surgical implantations [17,18]. Furthermore, the functional peptides are more preferred than their homological proteins in many applications as peptides can be modified by chemical methods without function loss but proteins are more sensitive and prone to denaturation under moderate or severe conditions.

Among the various strategies for functionalizing bone-implanted biomaterials, surface engineering shows superiority since it can provide site-specific therapies at implant-bone interface while maintaining the favorable properties of bulk materials [19–25]. If AMPs and OGP can be efficiently introduced onto the surface of PEEK implants, a dual-effect of anti-infection and osteo-induction can be anticipated. However, the PEEK material provides much better chemical resistance than most of other polymeric biomaterials, which poses a great obstacle to their surface functionalizations with biomolecules [26]. Although some solutions with strong reactivity such as concentrated sulfuric acid can be utilized to activate PEEK surface, such strategies are not delicate enough to make a balance between host defense and tissue repair and the residue of reactive agent may even raise the safety concern [27]. In this context, it is of great significance to develop simple and efficient strategies for the surface functionalization of PEEK biomaterials, in particular, achieving the anti-infective and osteo-inductive functions concurrently on these polymeric osteoimplants.

Inspired by the mussel adhesion mechanism, here we reported a biomimetic surface strategy for rational integration of anti-infectivity and osteo-inductivity onto PEEK implants in an optimized process using a catecholic amino acid (3,4-dihydroxy-L-phenylalanine, DOPA)-rich peptide with clickable azido terminal (Fig. 1A) [28]. The catecholic structures are versatile for adhering onto bulk materials and the design of clickable peptide mainly comes from the drawbacks of classical dopamine-based mussel surface chemistry, in which the second-step biomolecular conjugations *via* Michael addition or Schiff-base reaction will potentially compromise the functions of linked biomolecules by consuming their active sites (i.e., the amino and thiol groups) [29,30]. In

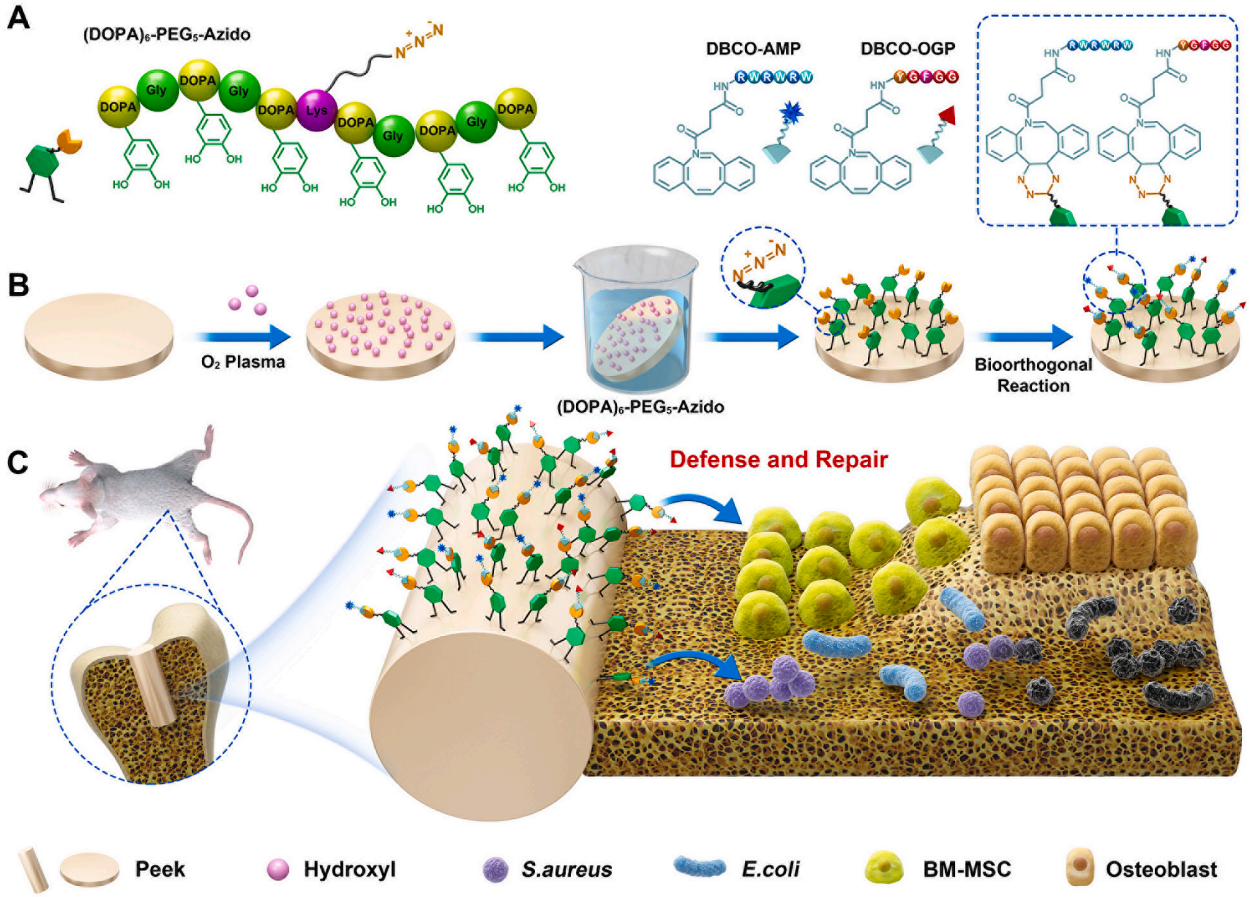

Fig. 1. Schematic illustration of biomimetic peptide clicking strategy. (A) The molecular structures of the clickable mussel-inspired peptide mimics and two DBCO-capped bioactive peptides with different functions. (B) The procedure of activating PEEK using the biomimetic peptide clicking strategy. (C) The PEEK implant functionalized with peptides shows a dual-effect of anti-infectivity and osteo-inductivity.

addition, the non-thoroughness and low specificity of these reactions will also take a toll on the reproducibility and controllability (i.e., the random molecular orientation and heterogeneous molecular mechanism) [31]. On the contrary, the clickable mussel-inspired peptide designed in our study enables bioorthogonal reaction (i.e., the dibenzylcyclooctyne (DBCO)-azido cycloaddition chemistry), showing various advantages including not only the mussel-like surface adhesion but also specificity, rapidity, thoroughness and biocompatibility in bioconjugations [32–34]. To match the dual-functional requirements of host defense and tissue repair, a typical AMP and the active sequence of OGP were synthesized and modified with bioorthogonally clickable group DBCO. In this case, PEEK surfaces can be rationally endowed with anti-infectivity and osteo-inductivity concurrently *via* a feeding-dependent bioorthogonal grafting process (Fig. 1B) [35]. Conceivably, the optimal performance of these two preferred functions for osteoimplants could synergistically contribute to a solid osseointegration of PEEK implants *in situ* even when confronting bacteria invasion (Fig. 1C). Furthermore, this work may provide a promising solution for surface bioengineering of other inert biomaterials, in particular, for the rational design of multifunctional surfaces with regard to the diversified clinical requirements.

2. Materials and methods

2.1. Materials

Peptides were prepared using standard Fmoc solid-phase synthesis. The PEEK discs (15 mm in diameter and 1.0 mm in thickness) were purchased from Waston Medical Appliance Co. (Changzhou, China), and PEEK rods (1.5 mm in diameter and 10 mm in length) were obtained from Tianzhu Changyun Medical Technology Co. (Beijing, China).

2.2. Characterization

High performance liquid chromatography (HPLC) was performed on a liquid chromatograph mass spectrometer (Ekspert™, Eksigent, USA). Electrospray ionization mass spectrometry (ESI-MS) was carried on an electrospray ionization mass spectrometer (API 4000+, SCIEX, USA). X-ray photoelectron spectroscopy (XPS) was conducted on the X-ray photoelectron spectrometer (K-Alpha, Thermo electronics, USA) and atomic force microscopy (AFM) images were obtained on an atomic force microscope (Dimension ICON, Bruker, USA). Stastic contact angle measurement was performed on the contact angle measuring instrument (OCTA21, DATAPHYSICS, Germany) using sessile distilled water under ambient conditions.

2.3. Surface functionalization

PEEK discs or rods was treated by O_2 plasma and then immersed in phosphate buffer saline (PBS) with the biomimetic peptide $(DOPA)_6$-PEG_5-Azido (0.01 mg/mL) for 15 min to obtain PEEK-Azido. The PEEK-Azido samples were then incubated with DBCO-AMP, DBCO-OGP or a mixture the two at a fixed total concentration of 0.1 mM in PBS. To obtain PEEK samples functionalized with different amount of AMP and/or OGP, we prepared five groups of PEEK samples with the DBCO-AMP/DBCO-OGP feeding molar ratios at 4:0, 3:1, 2:2, 1:3 and 0:4, and the modified samples were designated as PEEK-Azido, PEEK-A_4O_0, PEEK-A_3O_1, PEEK-A_2O_2, PEEK-A_1O_3 and PEEK-A_0O_4, respectively. After different surface functionalizations, the substrates were thoroughly rinsed with ultrapure water and then dried with nitrogen for the further use.

2.4. Cell culture

The bone marrow mesenchymal stromal cells (BM-MSCs) were obtained from the Shanghai Cell Bank of the Chinese Academy of Sciences, and cultivated in Dulbecco's modified Eagle's medium (DMEM, HyClone, USA) supplemented with 10% fetal bovine serum (FBS, Gibco, USA) and 1% penicillin/streptomycin (Gibco, USA). During the cell culture, the medium was refreshed every 3 days until a 70–80% of cell coverage on cell culture dish was reached. The cell seeding density was 2×10^4 cells per sample using 24-well plates as the holders.

2.5. Cytocompatibility

After culturing BM-MSCs on different PEEK samples for 24 h, a live/dead cell staining kit (AmyJet Scientific, Wuhan, China) was used for cell staining. In particular, both calcein AM (2×10^{-6} M) and EthD-1 (10×10^{-6} M) were utilized to stain the live cells in green and dead cells in red respectively, and the stained cells were observed under a laser confocal microscope (TCS SP8, Leica, Germany). Lactic dehydrogenase (LDH) and Cholecystokinin octapeptide (CCK-8) kits (Beyotime, China) were also used to determine the proliferation and cytotoxicity of BM-MSCs cultured on different samples. Briefly, BM-MSCs were cultured on different PEEK samples for 1, 3 and 5 days. Afterwards, the culture medium was collected, centrifugated and determined for the LDH activity by adding 10% LDH solution and measuring the absorbance at a wavelength of 490 nm on a full-wavelength plate reader (SuPerMax 3000 AL, FLASH, China) after 2 h of incubation. At the same timepoints, 200 μL of 10% CCK-8 solution were added to each sample and the absorbance at 450 nm was determined on a full-wavelength plate reader (SuPerMax 3000 AL, FLASH, China) after 2 h of incubation.

2.6. Cell adhesion and morphology

The BM-MSCs cultured on different samples were also determined by fluorescent staining. Briefly, after 48 h of cell culture, the cells on different samples were fixed with 4% paraformaldehyde for 30 min at 4 °C, and 0.1% Triton X-100 (Beyotime, China) was used to permeabilize the cells for 15 min. Subsequently, the cells were rinsed with PBS for 3 times and 10% bovine serum albumin (Beyotime, China) was used to block the non-specific binding sites. Each well was then cultivated with 250 μL of F-actin (1:200 dilution, Yeasen, China) at room temperature for 1 h, rinsed with PBS for 3 times, and alexa FluorTM 488 phalloidin (Thermo Fisher, USA) were added and incubated for another 1 h in dark. Afterwards, cells were counterstained with 4′,6-diamidino-2-phenylindole hydrochloride (DAPI, Beyotime, China) for 5 min, rinsed with PBS for 3 times, and then observed under a laser confocal microscope (TCS SP8, Leica, Germany). In addition to fluorescent staining, scanning electron microscopy (SEM) analysis was also performed to investigate the cell adhesion and morphology. After 1 and 3 days of cultivation, the cells on different samples were fixed with glutaraldehyde (2.5% v/v) for 2 h and dehydrated in gradient ethanol (20%, 40%, 60%, 80%, and 100%) for 15 min each. Subsequently, the different samples were vacuum-dried, sputter-coated with gold, and observed under field emission SEM (FE-SEM, S-4700, HITACHI, Japan).

2.7. In vitro antibacterial activity

S. aureus (ATCC 25923) and *E. coli* (ATCC 25922) were used for the antibacterial assay. Both bacteria strains were cultured in Luria-Bertani (LB) medium (Sigma-Aldrich, USA). Specifically speaking, the cryopreserved bacteria were recovered on LB agar plates for 24 h at 37 °C and sub-cultured twice. Afterwards, the bacteria were picked with the inoculating loop and dissolved in the LB medium to obtain the bacterial suspensions, and then diluted with sterile PBS to a concentration of $1 \times 10^{7-8}$ per mL. To observe the morphology of cultured bacteria, 500 μL of each bacterial suspension was seeded onto different substrates in 24-well plate and statically incubated at 37 °C for 6 h. After gently washing with PBS for 3 times, the adhered bacteria on different samples were fixed with paraformaldehyde (4 wt %) at 4 °C for 30 min, dehydrated with gradient ethanol (20%, 40%, 60%, 80%, and 100%) for 15

min each and further dehydrated with *tert*-butyl alcohol for another 30 min. Subsequently, the different samples were vacuum-dried, sputter-coated with gold, and the morphology of adhered bacteria were observed under FE-SEM (S-4700, HITACHI, Japan). The *in vitro* antibacterial efficiency was further determined by plate counting method. In particular, 100 μL of each bacterial suspension was seeded onto different samples in 24-well plate. The sample surfaces were then covered by a polyethylene film (1 cm × 1 cm) to ensure the sample-bacteria contact and statically incubated at 37 °C for 6 h. After the incubation, the cultured bacteria in different groups were detached from the sample surfaces by supersonic elution using sterile PBS containing 0.1% Tween 80 and the sample surfaces were rinsed with sterile PBS for 3 times. The bacterial eluent in different groups was diluted with sterile PBS to proper concentration, then 100 μL of the diluted bacterial eluent was spread on LB agar plates and incubated at 37 °C for 24 h. Afterwards, the number of colonies formed units (CFUs) was counted and imaged, and the antibacterial ratio was determined by the following formula: Antibacterial ratio = (A − B)/A × 100%, where A referred to the average CFUs of PEEK control group and B referred to the average CFUs of different experimental groups. The membrane permeability of bacteria in different groups was further evaluated using an ONPG assay (Sigma-Aldrich, USA). Typically, 500 μL of the bacterial suspension (1×10^6 per mL) was cultured on different substrates at 37 °C for 6 h and afterwards, the adhered bacteria were treated with 500 μL of O-nitrophenyl-*β*-D-galactopyranoside (ONPG) solution (0.75 M in NaH_2PO_4 buffer) for 2 h. The yellow supernatant in each well was determined for the absorbance at 405 nm on a spectrophotometric microplate reader (Bio-Rad 680, USA). Furthermore, the ATP levels of bacteria in different groups were evaluated using an ATP kit (Abcam, USA) according to the manufacturer's instructions.

2.8. In vitro osteogenic differentiation

For osteogenic differentiation, BM-MSCs were cultured on different PEEK substrates for 3 days and then the culture medium was refreshed with the osteogenic medium (DMEM supplemented with 0.1 μM dexamethasone, 50 μM ascorbic acid, 10 mM β-glycerol phosphate, and 10% FBS) for osteogenic culture. After 4, 7 and 14 days of osteogenic induction, the ALP activity of BM-MSCs on different samples was detected using an alkaline phosphatase (ALP) Kit (Beyotime, China) and normalized to the total protein content. For ALP staining, the cells after 14 days of osteogenic induction were rinsed with PBS for 3 times, fixed with paraformaldehyde (4 wt %) at 4 °C for 30 min, and then incubated in a 5-Bromo-4-Chloro-Indoly1 Phosphate/Nitroblue tetrazolium chloride (BCIP/NBT) working solution (Beyotime, China) in the dark for 20 min.

2.9. Matrix mineralization

After 7, 14 and 21 days of osteogenic culture, the cells cultured on different samples were fixed with 95% ethanol for 15 min and 40 mM Alizarin red S (ARS, Beyotime, China) was added for staining at room temperature for 30 min. Subsequently, the cells were washed 3 times with deionized water and observed by optical microscopy (DM750 M, Leica, Germany). In the quantitative assay, 10% (v/w) cetylpyridinium chloride (Sigma-Aldrich, USA) in sodium phosphate (pH 7.0) was added for 15 min and the eluted solution in different groups were measured for the absorbance at 570 nm.

2.10. Immunofluorescent staining

After 7 days of osteogenic culture, the BM-MSCs cultured on different groups were fixed with paraformaldehyde (4 wt %) at 4 °C for 30 min. Subsequently, 0.2% Triton X-100 (Beyotime, China) was added to permeabilize cells and all the samples were sealed with Blocking Buffer (Beyotime, China). Afterwards, primary antibodies were added into each well (anti-OCN, 1:200, Cell Signaling Technology, USA) for the incubation at 4 °C overnight. The cells were then rinsed with PBS for 3 times, and the corresponding fluorescent secondary antibody (Alexa Fluor 488, ab150077, Abcam, UK) was added for cultivation in the dark for 1 h. All the samples were counterstained with DAPI (Beyotime, China), placed on a microscope slide with fluorescence anti-fade medium (Beyotime, China), and observed under a laser confocal microscope (TCS SP8, Leica, Germany).

2.11. Quantitative reverse transcription polymerase chain reaction (qRT-PCR)

After 4, 7 and 14 days of osteogenic culture, the total RNA was extracted from BM-MSCs in different groups by adding Trizol reagent (Beyotime, China), and reversely transcribed into cDNA using a synthesis kit (Takara Bio, Japan). The gene levels of ALP, Runx2, COL1A1 and OCN were analyzed by qRT-PCR (S1000, Biorad, USA) using a mixture of dNTP reagent (TaKaRa, Japan) and RNase-free H_2O (Abcam, Cambrige, UK), as well as the forward and reverse primers listed below. The $2^{-\Delta\Delta CT}$ method was used to analyze gene expression data and glyceraldehyde phosphate dehydrogenase (GAPDH) gene was employed as the housekeeping gene for normalization.

ALP forward: 5′-GGGGTCAAAGCCAACTACAA-3′, ALP reverse: 5′-CTTCCCTGCTTTCTTTGCAC-3'; Runx2 forward: 5′-GCCGGGAATGATGAGAACTA-3′, Runx2 reverse: 5 ′ GGACCGTCCACTGTCACTTT-3′; COL1A1 forward: 5′-AATGGTGCTCCTGGTATTGC-3′, COL1A1 reverse: 5′-GGTTCACCACTGTTGCCTTT-3′; OCN forward: 5′-GAGGGCAGTAAGGTGGTGAA-3′, OCN reverse: 5′-GTCCGCTAGCTCGTCACAAT-3′; GAPDH forward: 5′- TGACCTCAACTACATGGTCTACA -3′, GAPDH reverse: 5′- CTTCCCATTCTCGGCCTTGTACA -3'.

2.12. In vivo modeling

65 Sprague Dawley rats (male, 6 weeks old, average weight = 300 ± 30 g) were randomly divided into five groups according to the employment of different implants: PEEK, PEEK-Azido, PEEK-A_4O_0, PEEK-A_0O_4 and PEEK-A_2O_2 (13 rats in each group). The animal protocol was approved by the Animal Ethics Committee of the First Affiliated Hospital of Soochow University (Suzhou, China). To construct implant-related infection model, *S. aureus* (2×10^3 bacteria in 20 μL of PBS) were evenly coated on different PEEK implants, and then the implants were placed in a wet environment at 37 °C for 4 h to allow bacteria adhesion. Afterwards, all the experimental rats received two implants in the distal femora under sterile conditions. At the beginning, general anesthesia of experimental rats was performed by intraperitoneal injection of 2% pentobarbital sodium (2 mL/kg, #P3761, Sigma-Aldrich, USA). Subsequently, a 10 mm of longitudinal incision was made along the medial side of the knee joint and the extensor mechanism with a patella was dislocated laterally. With the knee in flexion, a bone tube (1.5 mm in diameter and 12 mm in length) was drilled with a Kirschner wire from the intercondylar notch. Next, the PEEK implants in different groups were inserted into the medullary canal of the femur *via* distal femoral metaphysis until the implant end was below the articular surface. The patella was relocated and extensor mechanism was reconstructed. Finally, the soft tissues were sutured and the animals received intramuscular analgesic injection for 3 days after the operation. After 28 and 35 days post-implantation, calcein (10 mg/kg; #C0875, Sigma-Aldrich, USA) was intramuscularly administered into the experimental rats in different groups to label new bone formation.

2.13. In vivo anti-infection evaluation

After 2 weeks post-surgery, 20 rats (4 in each group) were euthanized with the overdose of pentobarbital and the femurs with different PEEK implants were harvested for the following performances. Firstly, to determine the number of viable bacteria in different groups, the

harvested implants were immersed with 1 mL of sterile PBS, sonicated for 10 min to detach the adhered bacteria and 10-times diluted with PBS. Afterwards, 100 μL of different diluents were spread on agar culture plates, and then cultured at 37 °C for 12 h. The visible bacterial colonies in different groups were imaged and recorded to calculate the antibacterial efficiency as described above. Moreover, the implants were immersed with 5 mL of MHB medium (Sigma-Aldrich, USA), cultured at 37 °C overnight, and then determined for the turbidity. The peri-implant soft tissues in different groups were carefully obtained and fixed in formaldehyde solution (4%) at 4 °C for 72 h. Meanwhile, all the collected femurs were fixed in formalin (10%) for 48 h, calcified in 10% ethylenediaminetetraacetic acid (EDTA, Sigma-Aldrich, USA) for 4 weeks, and the peri-implant bone tissues were obtained after removing the PEEK implants. After being rinsed with PBS for 3 times, the soft and bone tissues in different groups were dehydrated with a gradual ethanol solution (50%, 70%, 90%, 100% and 100%), infiltrated with xylene, embedded with paraffin and sectioned into 6 μm of slices for hematoxylin and eosin (H&E) and Giemsa staining. Finally, the stained sections were visualized by fluorescence microscopy (Axio Imager 2, Zeiss, Germany).

2.14. Osseointegration evaluation

After 6 weeks post-surgery, the other 45 rats (9 in each group) were euthanized with overdose of pentobarbital (Sigma-Aldrich, USA) and the femurs with different PEEK implants were harvested for the following performances. Firstly, the peri-implant bone tissues (n = 6 each group) were assessed by high resolution micro-CT (SkyScan1176, Aartselaar, Belgium) when the scanning parameters were set at 9 μm per layer under the voltage of 50 kV and with a current of 500 μA. A cylinder with a diameter of 1.7 mm and a length of 10 mm, located near the femur growth plate, was defined as the volume of interest for micro-CT analysis. 3D image reconstruction was performed and the morphometric parameters including bone mineral density (BMD), connectivity density (Conn.D), bone volume/total volume (BV/TV), bone surface/bone volume (BS/BV), and some other parameters such as trabecular number (Tb·N), trabecular thickness (Tb·Th) and trabecular separation (Tb.Sp) were systematically evaluated. In addition, the collected femurs (n = 4 per group) were assessed by the biomechanical push-out test using a material mechanical test system (Proline, Zwick, Germany). Initially, a 1 mm distal resection of femur metaphysis was performed to expose the PEEK rod. Prior to the biomechanical push-out test, dental cement was used to fix the femurs containing implants. The fixed samples were vertical to the bottom plane to ensure that the pushing force was parallel to the long axis of the implants. Afterwards, the implants were continuously pushed at a velocity of 1 mm per minute along the loading direction. During the process of push-out test, the load of force was recorded to identify the maximum fixation strength.

2.15. Histological immunofluorescent staining

Prior to the histological iemmunofluorescent staining, all the collected femurs were fixed in formalin (10%) for 48 h. Parts of the femurs (n = 6 per group) were sectioned into 1 mm of slices under undecalcified condition. Afterwards, the calcein double labeling in different groups was visualized by fluorescence microscopy (Axio Imager 2, Zeiss, Germany), and MAR was calculated. Part of the undecalcified sections were subjected to toluidine blue staining and visualized using a fluorescence microscope (Axio Imager 2, Zeiss, Germany). Rest of the femurs (n = 6 per group) were calcified in 10% EDTA (Sigma-Aldrich, USA) for 4 weeks, dehydrated with gradient ethanol, embedded with paraffin after removing the PEEK implants, and then sectioned into 6 μm of slices for H&E staining. The H&E stained sections were visualized by fluorescence microscopy (Axio Imager 2, Zeiss, Germany). Immunofluorescent staining was also performed to visualize the osteogenesis-related markers. At first, the primary antibodies of Runx2 (ab192256, Abcam, UK), Osterix (ab22552, Abcam, UK) and OCN (orb1266, Biorbyt, UK) were added for 12 h of incubation at 4 °C. Afterwards, the sections were rinsed and the corresponding fluorescent secondary antibodies (Alexa Fluor 647 and Alexa Fluor 488) were added for another 1 h of incubation in the dark. All the sections were counterstained with DAPI (Beyotime, China), and then observed under a fluorescence microscope (Axio Imager 2, Zeiss, Germany). The fluorescence intensity was assessed using image J software (Bethesda, USA).

2.16. Statistical analysis

The values were represented as means ± standard deviation. The student's t-test was performed to compare the differences between two groups and one-way analysis of variance followed by Tukey's test was performed to make multiple comparisons. A difference at $*p < 0.05$ was considered to be significant and that at $\#p < 0.01$ was considered to be highly significant.

3. Results

3.1. Peptide synthesis and surface functionalizations

The mussel-inspired clickable peptide was synthesized by a solid-phase peptide synthesis strategy according to our previous reports [36–38]. Briefly, 3,4-dihydroxy-L-phenylalanine (DOPA), a catecholic amino acid abundant in mussel foot proteins (Mfps), was introduced into the peptide sequence by using acetonide-protected Fmoc-DOPA (acetone)-OH [39]. To facilitate mussel-like molecular adhesion onto substrates and leave accessible groups for the second-step bioorthogonal reaction, hexavalent DOPA units with one lysine interval and a polyethylene glycol (PEG)-linked azido were integrated to obtain the clickable catecholic peptide ($(DOPA)_6$-PEG_5-Azido) (Fig. 1A and Fig. S1). On the other hand, a typical antimicrobial peptide (RWRWRW) and the active sequence of osteogenic growth peptide (YGFGG) were selected and capped with DBCO *via* *N*-hydroxysuccinimide-amine and maleimide-thiol coupling, respectively (Fig. S1) [40]. The obtained DBCO-capped antimicrobial peptide (DBCO-AMP) and osteogenic growth peptide (DBCO-OGP) thus could be grafted onto the surfaces functionalized with $(DOPA)_6$-PEG_5-Azido *via* bioorthogonal reaction, achieving a tunable dual-functional surface modification. HPLC analysis showed that all the three synthetic peptides were high in purity (>96%) (Fig. 2A). The peptides were also characterized with ESI-MS to confirm their molecular structures. As shown in Fig. 2B, the $[M+H]^+$ and $[M+2H]^{2+}$ of $(DOPA)_6$-PEG_5-Azido were found at 1809.32 and 905.28 Da, respectively, which were corresponding to its theoretical molecular weight at 1808.80 Da. Likewise, the detected molecular ion peaks of DBCO-AMP and DBCO-OGP were also corresponding to their theoretical molecular weight at 1315.68 and 788.34 Da, respectively. These results demonstrated the successful synthesis of clickable mussel-inspired peptide and the complementary DBCO-capped bioactive motifs.

Since the multivalent catecholic molecules enable easy and stable binding onto a wide range of materials through mussel-like molecular adhesion, the PEEK discs pre-activated by O_2 plasma were used as the substrates for peptide binding and biomolecular grafting. Briefly, the PEEK substrates were first coated with the mussel peptide $(DOPA)_6$-PEG_5-Azido in PBS solution, and then incubated with different ratios of DBCO-AMP and DBCO-OGP for further dual-functionalization through the bioorthogonal DBCO-Azido click reaction. After sample preparation, the surface elemental compositions of bare PEEK, azido-modified PEEK (PEEK-Azido), and the samples functionalized with different ratios of DBCO-AMP and DBCO-OGP (PEEK-A_4O_0, PEEK-A_2O_2 and PEEK-A_0O_4, the subscripted numbers denoting the ratios of DBCO-AMP and DBCO-OGP) were analyzed by XPS. As shown in Fig. 2C and D, an enhanced signal of N1s around 400 eV was detected on the azido-modified PEEK substrate, which could be further increased after the subsequent functionalizations with DBCO-AMP and/or DBCO-OGP. Since PEEK is a

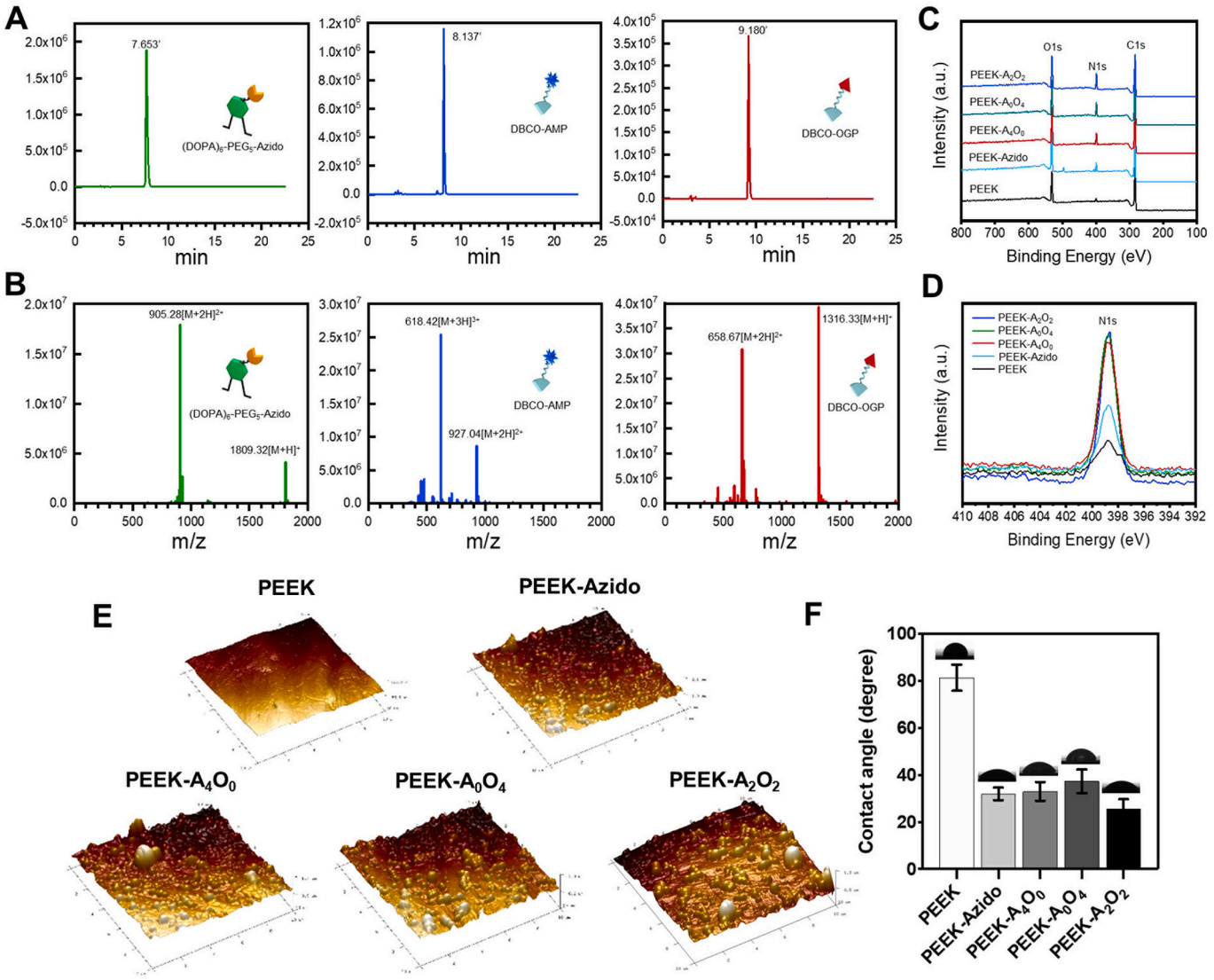

Fig. 2. Peptide synthesis and surface functionalizations. (A, B) HPLC analysis and ESI mass spectra of $(DOPA)_6$-PEG_5-Azido, DBCO-AMP and DBCO-OGP. (C, D) XPS analysis of different PEEK substrates. (E, F) AFM images and water contact angles of different PEEK substrates.

nitrogen-free material, this result indicated the successful grafting of $(DOPA)_6$-PEG_5-Azido onto PEEK substrates, which could enable the second-step bioorthogonal conjugations with DBCO-capped bioactive peptides.

In addition to surface elemental analysis, the surface roughness and wettability of various samples were further characterized by AFM and water contact angle measurement, respectively [41]. As shown in Fig. 2E, the surface roughness of PEEK was significantly increased after peptide treatments. The bare PEEK substrate showed a relatively smooth surface morphology with roughness (R_a) at 22.25 ± 3.62 nm. After azido-modification, small but dense particles could be observed on the sample surface with the R_a value being increased to 53.53 ± 4.42 nm. Moreover, the second-step bioorthogonal peptide conjugations further increased the *R*a value of modified samples up to 67.07 ± 5.12 nm, and no significant difference of surface roughness could be detected among the PEEK-A_4O_0, PEEK-A_2O_2 and PEEK-A_0O_4. In addition to surface roughness, water contact angle measurements corroborated the successful process of biomimetic peptide adhesion and bioorthogonal conjugations [42]. Fig. 2F showed that the water contact angles of bare PEEK was around 80°, whereas those detected on the modified samples were below 40°. The significant decrease of water contact angles after surface modifications could be ascribed to the high hydrophilicity of $(DOPA)_6$-PEG_5-Azido and DBCO-capped peptides. These results demonstrated the great potential of our biomimetic peptide clicking strategy for the surface functionalizations of PEEK substrates.

3.2. *In vitro cytocompatibility*

As is known to all, cytocompatibility is the prerequisite of implanted biomaterials, and the desirable osteoimplants should be favorable to osteoblasts and their precursors [43–45]. In this regard, BM-MSCs were utilized to evaluate the cell adhesion and proliferation on PEEK substrates before and after surface functionalization [46]. Initially, BM-MSCs cultured on various samples were determined by living/dead staining [47]. It was clear in Fig. 3A that all the modified samples (PEEK-Azido, PEEK-A_4O_0, PEEK-A_3O_1, PEEK-A_2O_2, PEEK-A_1O_3 and PEEK-A_0O_4) provided better cytocompatibility than the bare PEEK substrate with negligible dead cells being found on them after 4 days of culture. CCK-8 assay and LDH assay were also performed to verify the good cytocompatibility of modified samples. As shown in Fig. 3B and C, all the peptide-coated PEEK substrates were superior to the bare one for better supporting the cell proliferation of BM-MSCs and lowering the cytotoxicity. Furthermore, the BM-MSCs cultured on various samples were determined by SEM and CLSM after cytoskeleton staining [48].

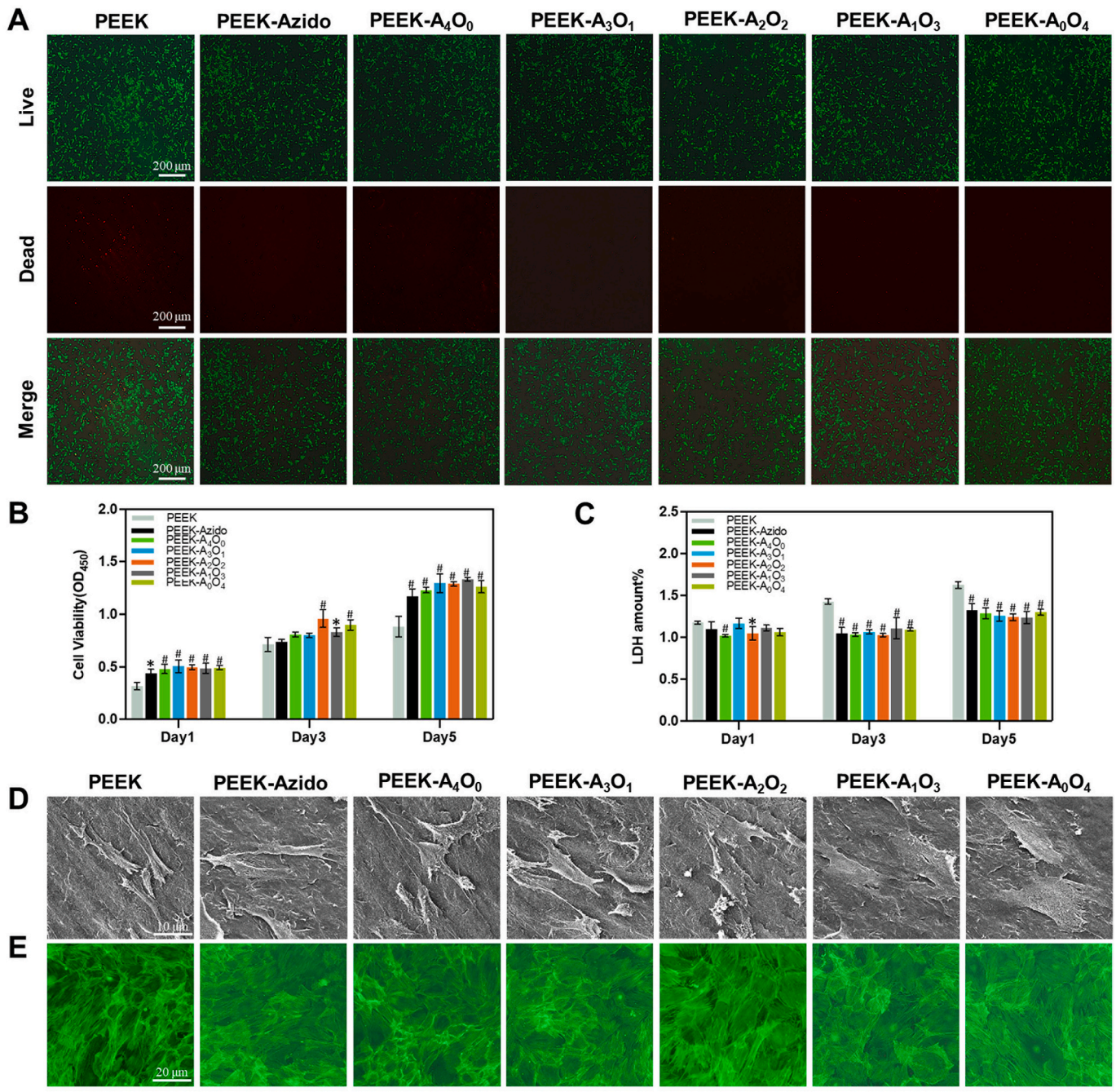

Fig. 3. Surface cytocompatibility. (A) Living/dead staining of BM-MSCs on different PEEK samples (Scale bar = 200 μm). (B, C) Cell viability and cytotoxicity of BM-MSCs cultured on different PEEK samples for 1, 3 and 5 days (n = 6 per group). (D, E) Typical SEM and CLSM images of adhered BM-MSCs in different groups (scale bar = 10 μm and 20 μm, respectively). Statistically significant differences were indicated by *p < 0.05 and #p < 0.01 compared with the bare PEEK group.

Fig. 3D showed that the BM-MSCs on peptide-modified samples were more extended as compared with those cultured on bare PEEK. In addition, clear cytosolic actin backbone and cell-to-cell contact could be observed in the modified groups (Fig. 3E). Overall, the biomimetic peptide coatings on PEEK substrates could significantly improve the adhesion and proliferation of BM-MSCs, reduce potential cytotoxicity, and promote the intercellular connection. These positive effects would be beneficial to the peri-implant tissue reconstruction *in vivo* as anticipated.

3.3. In vitro antibacterial activity

Since anti-infection has been considered as one of the critical activities for PEEK osteoimplants, the various PEEK substrates were then evaluated for their antibacterial effect using gram-negative *E. coli* and gram-positive *S. aureus* as the model bacteria [49]. At first, the bacteria were cultured on different PEEK samples for 12 h and then harvested for solid culture on agar plates. As shown in Fig. 4A, all the AMP-containing samples (PEEK-A_4O_0, PEEK-A_3O_1, PEEK-A_2O_2 and PEEK-A_1O_3) could inhibit the growth of bacteria as compared to bare PEEK. Moreover, the antibacterial efficiency of different groups exhibited an AMP-dependent manner, in which the higher AMP feeding ratio led to better bacterial inhibition. Quantitative analysis was then performed, and the result corroborated the AMP-dependent antibacterial activity (Fig. 4C). When the AMP/OGP feeding ratio was at 4:0 or 3:1 (PEEK-A_4O_0 and PEEK-A_3O_1), the peptide-modified samples showed a high antibacterial

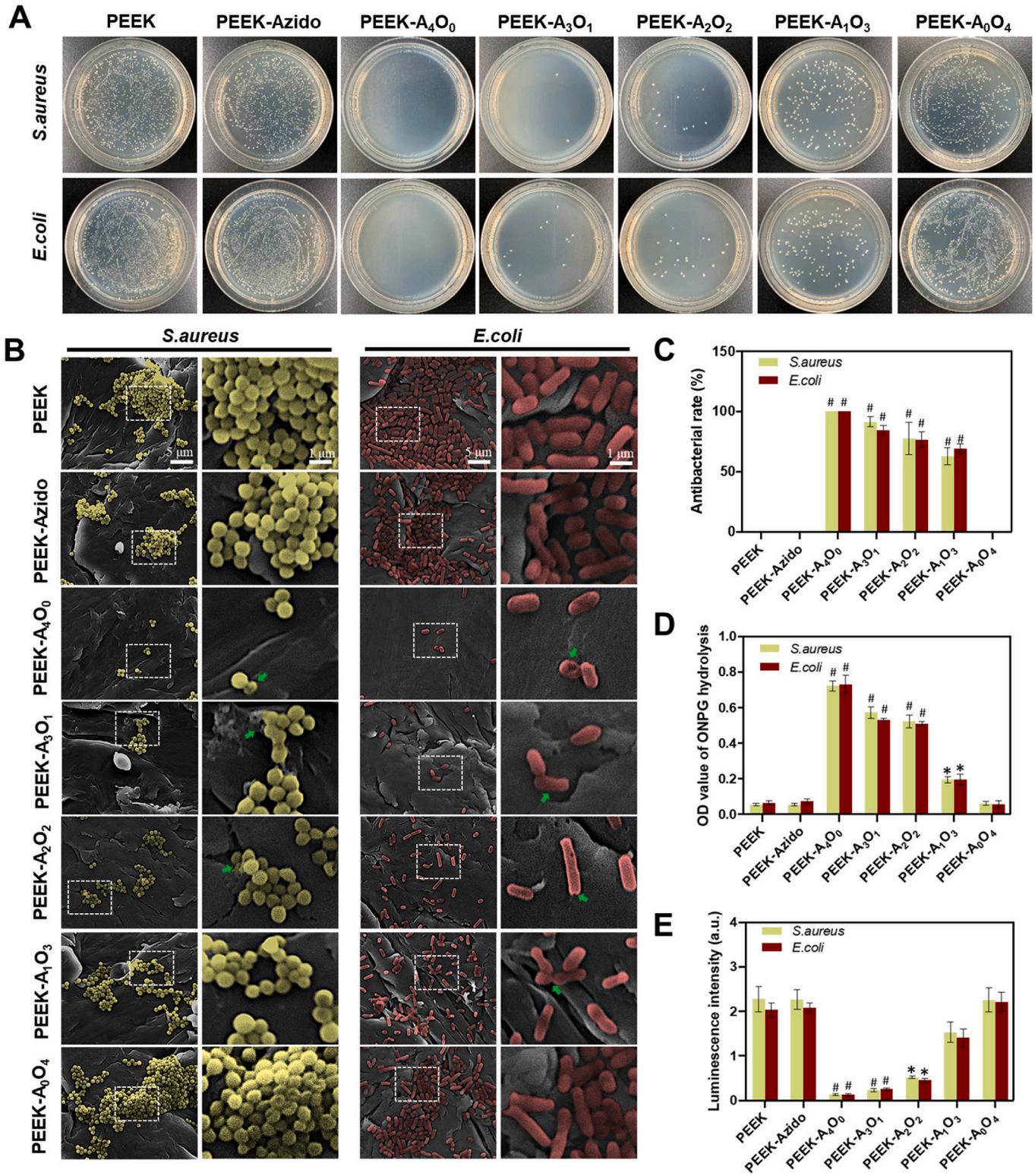

Fig. 4. In vitro antibacterial activity. (A) Solid culture after incubating E. coli and S. aureus (10^7 per mL) on different samples for 12 hours. (B) FE-SEM images of S. aureus and E. coli cultured on different surfaces (scale bar = 5 μm and 1 μm, respectively). S. aureus was labelled with yellow color and *E. coli* was red. The damages of cell walls were marked by green arrows. (C) Antibacterial activity of different groups determined by counting the bacterial colonies (n = 4 per group). (D) The results of ONPG hydrolysis assay (n = 4 per group). (E) The results of ATP test (n = 4 per group). Statistically significant differences were indicated by $^{*}p < 0.05$ and $^{\#}p < 0.01$ compared with the bare PEEK group.

rate > 90% against both *E. coli* and *S. aureus*.

Previous studies had demonstrated that AMP can punch the cell walls of bacteria and induce bacterial lysis [50]. Thus, FE-SEM was utilized to observe the morphologies of bacteria on different samples. As shown in Fig. 4B, both *E. coli* and *S. aureus* could maintain normal spherical and rod shapes on the PEEK, PEEK-Azido and PEEK-A_0O_4 samples. In contrast, the status of *S. aureus* and *E. coli* was deteriorated and their cell walls were contracted and deformed (see arrows in Fig. 4B) when being seeded onto the AMP-containing substrates (PEEK-A_4O_0, PEEK-A_3O_1, PEEK-A_2O_2 and PEEK-A_1O_3). These results indicated that the bacteria underwent a disruptive effect by the surface tethered AMP. To further verify the breakage of bacterial cell walls, ONPG was utilized to evaluate the membrane permeability of bacteria after different treatments [51]. This is because ONPG can react with the intracellular β-D-galactosidase to form yellow O-nitrophenol with strong absorption peak at 405 nm, and the more severe bacterial membrane is damaged, the stronger absorption at 405 nm can be observed [52]. As shown in Fig. 4D, the levels of ONPG hydrolysis in all the AMP-containing groups were significantly higher than those of the APM-free groups. Moreover, an AMP-dependent manner of ONPG hydrolysis was also found, which was in line with the previous antibacterial results. Since the damage of bacterial cell walls would probably lead to the leakage of cellular components and affect energy metabolism, the ATP levels in different groups were further determined using an ATP assay kit [53]. As expected, a gradually decreased ATP levels were detected in groups with increased AMP-feeding ratios (Fig. 4E). Taken together, the AMP-containing

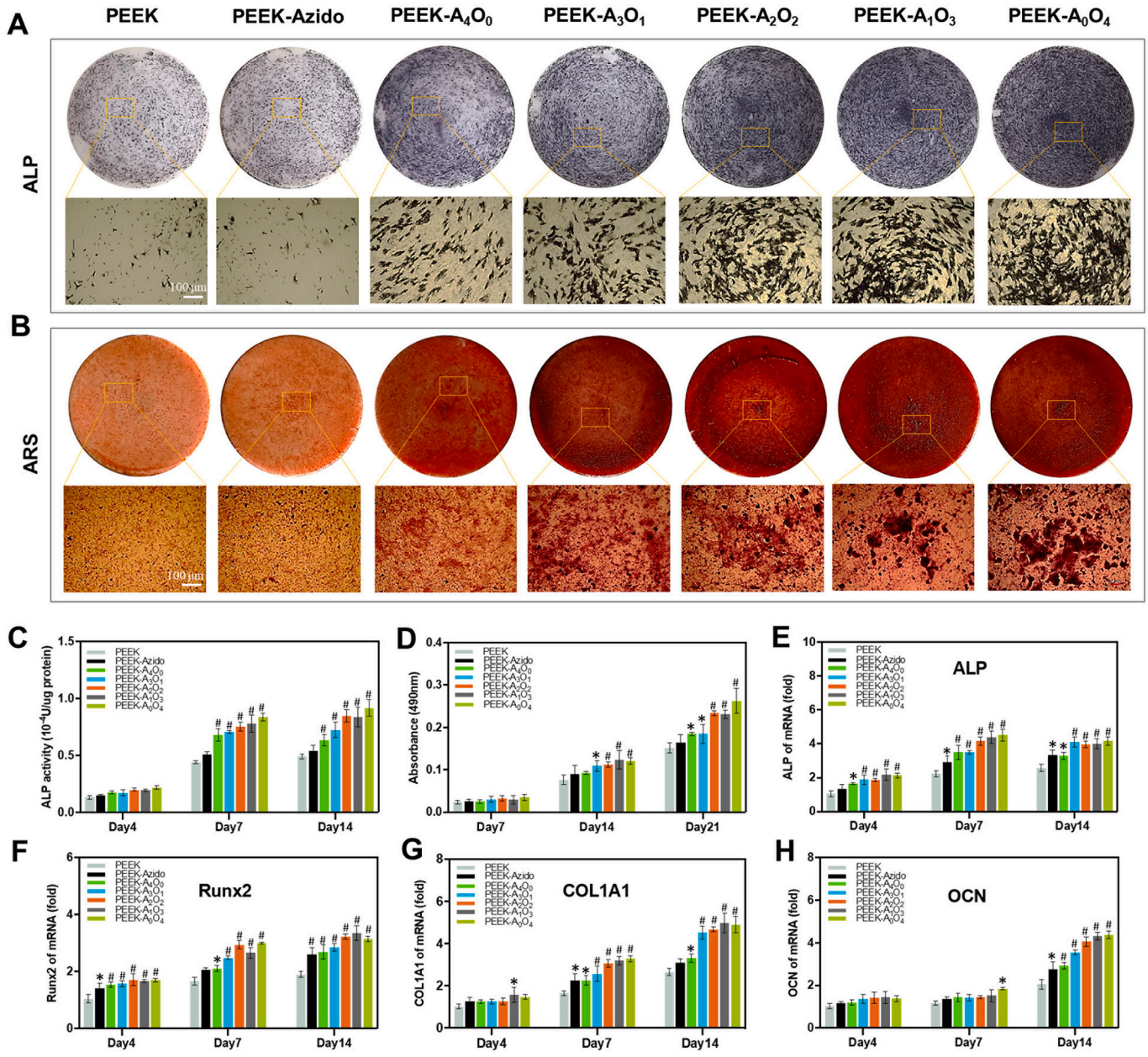

Fig. 5. In vitro osteogenic differentiation. (A) ALP staining of BM-MSCs on different samples after 14 days of osteogenic induction (Scale bar = 100 μm). (B) ARS staining of BM-MSCs on different samples after 21 days of osteogenic induction (Scale bar = 100 μm). (C) Quantitative analysis of ALP activity in different groups after 4, 7 and 14 days of osteogenic induction (n = 6 per group). (D) Semi-quantitative analysis of ARS staining in different groups after 7, 14 and 21 days of osteogenic induction (n = 6 per group). (E–H) Gene expressions of osteogenesis-related proteins including ALP, Runx2, COL1A1 and OCN of BM-MSCs in different groups after 4, 7 and 14 days of osteogenic induction (n = 6 per group). Statistically significant differences were indicated by *$p < 0.05$ and $^{\#}p < 0.01$ compared with the bare PEEK group.

samples were well demonstrated for their antibacterial effects.

3.4. In vitro osteogenic differentiation

The ideal osteoimplants should also provide sufficient osteogenic activity to achieve stable bone-implant integration [54,55]. Therefore, a series of *in vitro* tests were performed to evaluate the osteogenic ability in different groups. Initially, the BM-MSCs cultured on various substrates were determined for the ALP activity (an early marker of the metabolic activity of osteoblasts) after 4–14 days of osteogenic induction [56]. As shown in Fig. 5A, all the peptide-modified PEEK substrates could up-regulate the ALP activity of cultured cells, and the quantitative analysis showed that higher OGP feeding ratio led to higher ALP activity (Fig. 5C). After 7–21 days of osteogenic induction, the osteogenic differentiation in different groups was also evaluated by staining the cells with ARS. It was clear that all the OGP-containing groups (PEEK-A_3O_1, PEEK-A_2O_2, PEEK-A_1O_3 and PEEK-A_0O_4) could significantly increase matrix mineralization of cells after osteogenic induction (Fig. 5B), and the bone mineralization also showed an OGP-ratio-dependent manner (Fig. 5D).

To further explore the osteogenic differentiation of BM-MSCs on different samples, the gene expressions of osteogenesis-related proteins including ALP (an early marker of osteoblast differentiation), runt-related transcription factor 2 (Runx2, a pivotal translation factor in regulating osteoblastic function), type I collagen (COL1A1, the most significant component of collagen fiber in the bone matrix) and osteocalcin (OCN, the main component of bone non-collagenous protein) were analyzed by performing qRT-PCR after 4–14 days of osteogenic induction [57,58]. As shown in Fig. 5E–H, all the 4 kinds of gene expressions related to osteogenic differentiation were upregulated in the OGP-containing groups as compared to those in the other groups, which corroborated the OGP-dependent osteogenic activity. As the most specific marker in osteogenic differentiation, the OCN level in different groups was also determined by immunofluorescence staining. The representative immunofluorescence staining images were shown together in Fig. S2, which was in line with the result of OCN gene expression. Taken together, the OGP-containing groups were well demonstrated for their enhanced osteogenic ability *in vitro*.

3.5. Comprehensive analysis of in vitro results

Through the comprehensive evaluation of above *in vitro* results, it was clear that the biomimetic surface strategy employed in our study was effective for the surface functionalizations of PEEK implants with osteogenic and/or antibacterial properties. On one hand, the increase of OGP ratio could benefit the osteogenic differentiation of BM-MSCs. On the other hand, the decrease of AMP ratio during surface functionalization would inevitably compromise the antibacterial properties. The contrary tendency of anti-infectivity and osteo-inductivity thus compelled us to make a comprehensive consideration of the surface functions. To obtain an optimal condition of AMP/OGP co-grafting, a whole date analysis on the antibacterial and osteogenic effects in different groups was performed, and a heat map with various normalized properties was drawn for analysis (Fig. 6A). The groups with significant differences compared to the control group of bare PEEK were indicated by $^{*}p < 0.05$ and $^{\#}p < 0.01$. The heat map showed that the group of PEEK substrates with an AMP/OGP feeding ratio at 2:2 (PEEK-A_2O_2) provided the most comprehensive superiorities including good cytocompatibility, enhanced osteogenesis, and sufficient antibacterial activity as compared to the other groups.

Therefore, this optimal AMP/OGP co-modified condition was chosen for this surface functionalization of PEEK rods for the following bone implantation and *in vivo* assessments.

3.6. In vivo antibacterial activity

In clinic, the region of implantation is susceptible to bacterial infection due to the local granulocyte defects [59]. Despite the extensive use of antibiotics in the perioperative period, the implant-related infections are serious complications that commonly happen. In this respect, the optimal AMP/OGP co-modified sample was then evaluated for its anti-infective activity *in vivo*. The implanted samples were divided into five different groups as PEEK, PEEK-Azido, PEEK-A_4O_0, PEEK-A_0O_4, and PEEK-A_2O_2. An implant-related infection model was established

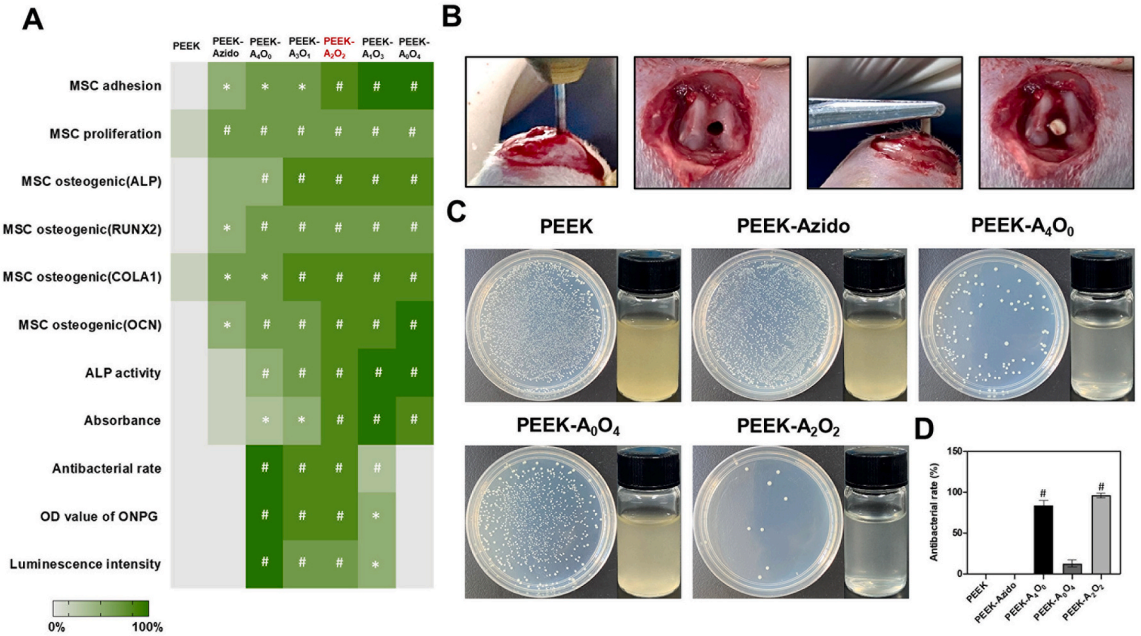

Fig. 6. (A) Comprehensive analysis of the *in vitro* performances of different PEEK samples in a heat map. Green denotes high activity and white denotes low. (B–D) In vivo antibacterial assessments after 2 weeks of implantation. (B) Establishment of implant-related infection model. (C) Photographs of bacterial colonies in different groups (left) and the media cultured with different implants for 12 h (right). (D) Quantitative analysis of antibacterial efficiency by counting the bacterial colonies in different groups (n = 4 per group). Statistically significant differences were indicated by $^{*}p < 0.05$ and $^{\#}p < 0.01$ compared with the bare PEEK group.

utilizing *S. aureus*-contaminated PEEK rods (Fig. 6B). Before implantation, two thousand *S. aureus* in solution were evenly spread on the implants in different groups. The *S. aureus*-contaminated PEEK rods were then implanted into the femurs of rats and after 2 weeks of implantation, the experimental rats were sacrificed. To evaluate the antibacterial performance *in vivo*, some symptoms of the rats including (1): the healing situation, (2) swelling around the implants, and (3) pus secretion in soft tissue or bone marrow cavity were monitored post implantation [60–62]. Fig. S3 showed that the experimental rats in PEEK-A_2O_2 group had a better wounding-healing than those in PEEK group, and there was no obvious swelling and pus in the peri-implant soft tissues of PEEK-A_2O_2 group.

To qualitatively evaluate the anti-infective performances of implants in each group, the PEEK rods in the femurs of rats were taken out, and then placed in 5 mL of Mueller-Hinton Broth (MHB) medium and cultivated at 37 °C overnight. As shown in Fig. 6C, the media in groups of PEEK-A_4O_0 and PEEK-A_2O_2 were clear and transparent. On the contrary, turbid media were observed in all the AMP-free groups (PEEK, PEEK-Azido, and PEEK-A_0O_4), indicating the abundance of viable bacteria on the implants. Furthermore, the bacteria adhered on different PEEK rods were subjected to ultrasonic vibration treatment for detachment, diluted in PBS, and then incubated on an agar plate at 37 °C for 12 h to determine the bacterial colonies. It was clear that the bacterial colonies in the PEEK-A_4O_0 and PEEK-A_2O_2 groups were significantly less than those observed in the other groups (Fig. 6C). Moreover, the quantitative result in Fig. 6D showed that PEEK-A_2O_2 could even provide a better antibacterial efficiency (96%) than the PEEK-A_4O_0 implants only modified by DBCO-AMP (81%). This is probably due to the anti-infective and osteo-inductive dual-effect of PEEK-A_2O_2, which could jointly contribute to a beneficial microenvironment for osteoimplants. Overall, our results demonstrated that the bacterial contamination on PEEK osteoimplants could be efficiently eliminated using our biomimetic peptide clicking strategy.

In the next step, both H&E staining and Giemsa staining were performed to evaluate the infiltration of inflammatory cells and bacteria in peri-implant tissues [63]. H&E staining showed that neutrophils could penetrate into the peri-implant soft tissues in the groups without AMP (PEEK, PEEK-Azido and PEEK-A_0O_4), and many bacteria were observed in the corresponding images after Giemsa staining (Fig. 7A). Simultaneously, there were a lot of neutrophils infiltrating around the implants in these groups, and bacteria were detected in bone tissues and around the bone marrow cavities (Fig. 7B). These results indicated that the PEEK, PEEK-Azido, and PEEK-A_0O_4 implants did not possess antibacterial activity and hence severe bacterial infections occurred in these groups. In contrast, only a few neutrophils and almost no bacteria could be detected in the PEEK-A_4O_0 and PEEK-A_2O_2 groups, further verifying the efficient anti-infection and minimal inflammatory response around the AMP-modified implants. Additionally, no tissue damage could be found in the main organs (heart, liver, spleen, lung and kidney) of experimental mice (Fig. S4), which indicated the absence of systemic side effects after bone implantation. In a word, our biomimetic peptide clicking strategy provided good biosafety, and sufficient anti-bacterial performances could be achieved *in vivo* when decorating PEEK implants with AMP.

3.7. In vivo interfacial osteogenesis

To further investigate the application prospects of our biomimetic peptide clicking strategy, the *in vivo* osteogenic performances of various PEEK implants were studied using the same implant infection model [64,65]. After 6 weeks of implantation, the bone tissues with implants were harvested from the experimental mice, sectioned into slices and then subjected to H&E staining and toluidine blue staining. As shown in Fig. 8A and Fig. 8B, fibrous layers were formed around the PEEK, PEEK-Azido and PEEK-A_0O_4 implants and the peri-implant bone mass was limited, which could be ascribed to the negative effect of bacterial infection in these groups. In contrast, the PEEK-A_4O_0 and PEEK-A_2O_2 implants introduced more and denser trabecular bone forming around as most of the peri-implant bacteria hampering osteogenesis had been eliminated by the decorated AMP. Furthermore, the PEEK-A_2O_2 group was superior to the PEEK-A_4O_0 group with regard to the osteogenic activity of OGP. Quantitative analysis brought to light that the

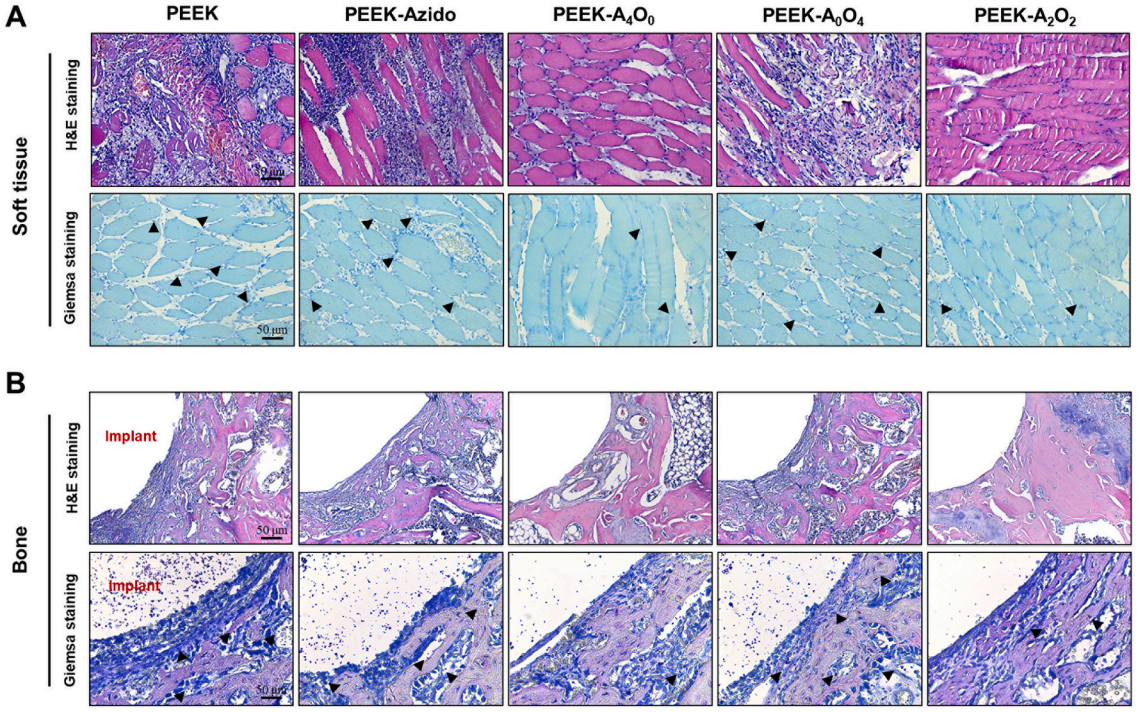

Fig. 7. In vivo assessments after 2 weeks of implantation. (A) H&E staining and Giemsa staining of the peri-implant Soft tissues (Scale bar = 50 μm). (B) H&E staining and Giemsa staining of the peri-implant bone tissues. Black arrows indicated bacteria (scale bar = 50 μm).

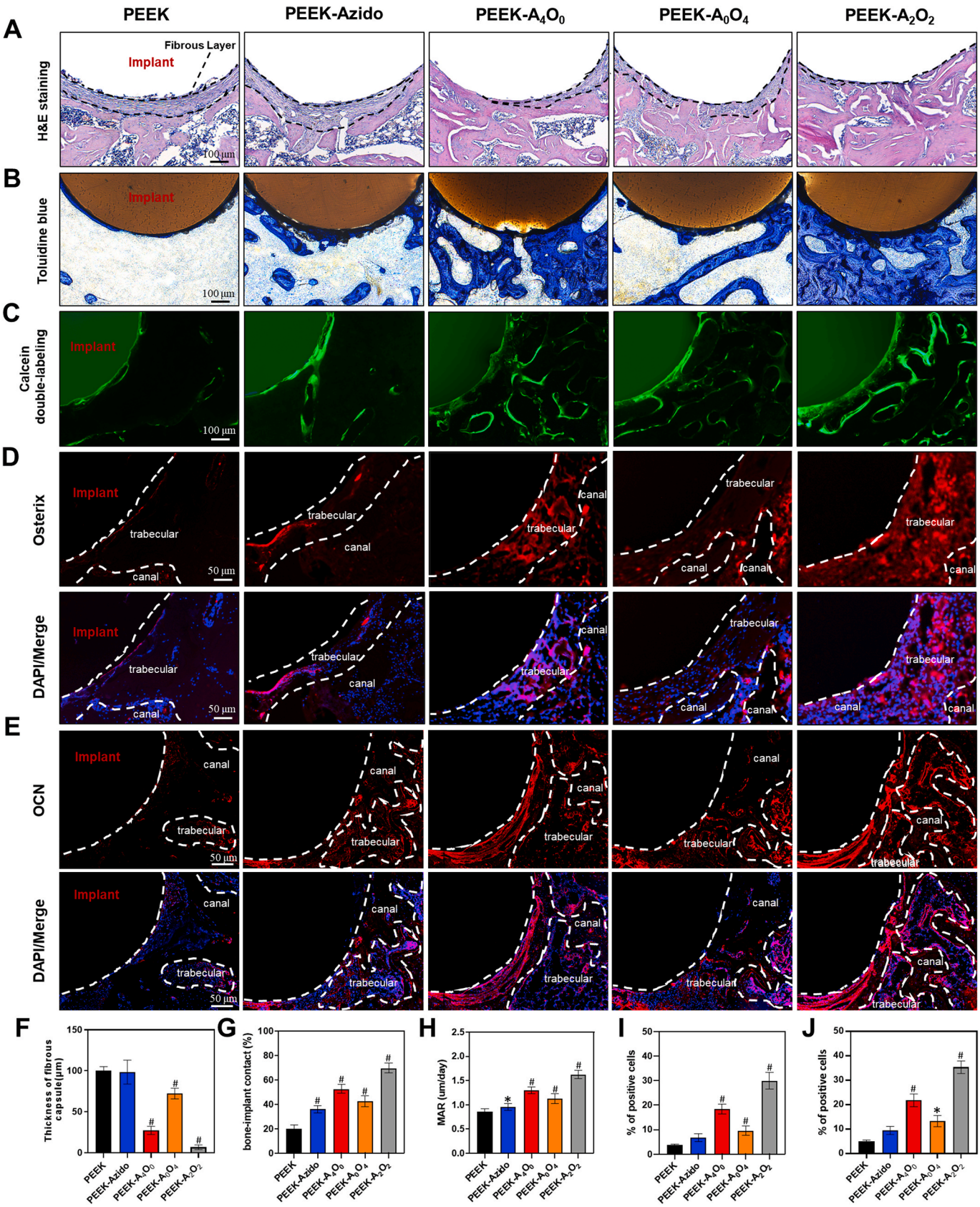

Fig. 8. In vivo osteogenic assessments after 6 weeks of implantation. (A–C) H&E staining, Toluidine blue staining and Calcein double-labeling of the peri-implant tissues in different groups (scale bar = 100 μm). (D, E) Immunofluorescent staining of the peri-implant tissues in different groups in red (Osterix, OCN) and blue (nuclei) fluorescence with white dotted lines indicating the contour distribution (scale bar = 50 μm). (F–J) Quantitative analysis of the thickness of fibrous capsule, BIC, MAR and percentage of Osterix and OCN positive cells (n = 6 per group). Statistically significant differences were indicated by $^{*}p < 0.05$ and $^{\#}p < 0.01$ compared with the bare PEEK group.

decoration of both AMP and OGP peptides could accelerate interfacial osteogenesis of PEEK implants by reducing the thickness of fibrous capsule (Fig. 8E) and improving bone-implant contact (BIC) (Fig. 8G). The BIC ratio of PEEK-A_2O_2 group was more than 3-folds as that of the PEEK group (Fig. 8G). Once again, these results corroborated that the dual-effect of host defense and tissue repair designed in our study was desirable, which could synergistically enhance the osseointegration of osteoimplants even under the condition of postoperative infection.

Furthermore, calcein double labeling was performed to assess the peri-implant mineral apposition and osteoblast formation in different groups [66]. It was clear that the PEEK implants in the PEEK-A_4O_0 and PEEK-A_2O_2 groups could induce more new bone mineralization than those in other groups without AMP (PEEK, PEEK-Azido and PEEK-A_0O_4) (Fig. 8C), and the mineral apposition rate (MAR) was significantly enhanced (Fig. 8H). In addition to mineral apposition, immunofluorescent staining was also performed to evaluate the *in vivo* osteogenesis in different groups. In the process of bone construction, Osterix is a zinc finger-containing transcription factor essential for the differentiation of osteoblasts, and Runx2 is a master transcription factor regulating the skeletal development [67]. It was clear that the early and later osteogenic markers including Osterix (Fig. 8D and I), Runx2 (Fig. S5) and OCN (Fig. 8E and J) were all up-regulated in the PEEK-A_4O_0 and PEEK-A_2O_2 groups, which corroborated that the circumvention of bacterial infection is a prerequisite for the following peri-implant osteogenesis. Noteworthily, the PEEK-A_2O_2 group provided the best osteogenic performances with regard to the highest MAR and expression of osteogenic transcription factors *in vivo*, and hence the synergistic effect of anti-infection and osteo-induction using our biomimetic peptide clicking strategy was verified.

To get a panoramic view of the peri-implant osseointegration, the femurs containing implants in different groups after 6 weeks of implantation were scanned by micro-CT for the analysis and evaluation of interfacial osteogenesis [68]. Fig. 9A showed the vertical and cross sections of femurs containing different implants as well as the micro-CT images after 3D reconstruction. Obviously, the newly formed bone surrounding the PEEK-A_4O_0 and PEEK-A_2O_2 implants was much denser than that observed in the other groups. The quantitative analysis on BMD, Conn. D, BV/TV, BS/BV, Tb·N, Tb·Th and Tb. Sp all showed that the AMP-modified implants were more conducive than the other implants to peri-implant bone regeneration, which was in line with the *in vivo* osteogenic results as mentioned above (Fig. 9B–H). As expected, the implants in the PEEK-A_2O_2 group showed the best interfacial osteogenesis among all. Since a stable connection between the implant and peripheral bone tissue is critical to the clinical prosperity of osteoimplants, the anchoring forces of different implants in femurs were then assessed by a mechanical push-out test illustrated in Fig. S6 [69]. As shown in 9I, the PEEK-A_2O_2 implants provided better mechanical stability than those in the other groups as the maximum pushing force was significantly improved. The results definitely verified the enhanced interfacial fixation strength of PEEK implants after surface functionalization with AMP and OGP. On the whole, our study demonstrated that the biomimetic peptide clicking method enabled rational design of anti-infective and osteo-inductive dual-effect on PEEK implants, which would facilitate high quantity and continuity of peri-implant bone formation *in vivo* and improve mechanical fixation even when confronting bacterial invasion.

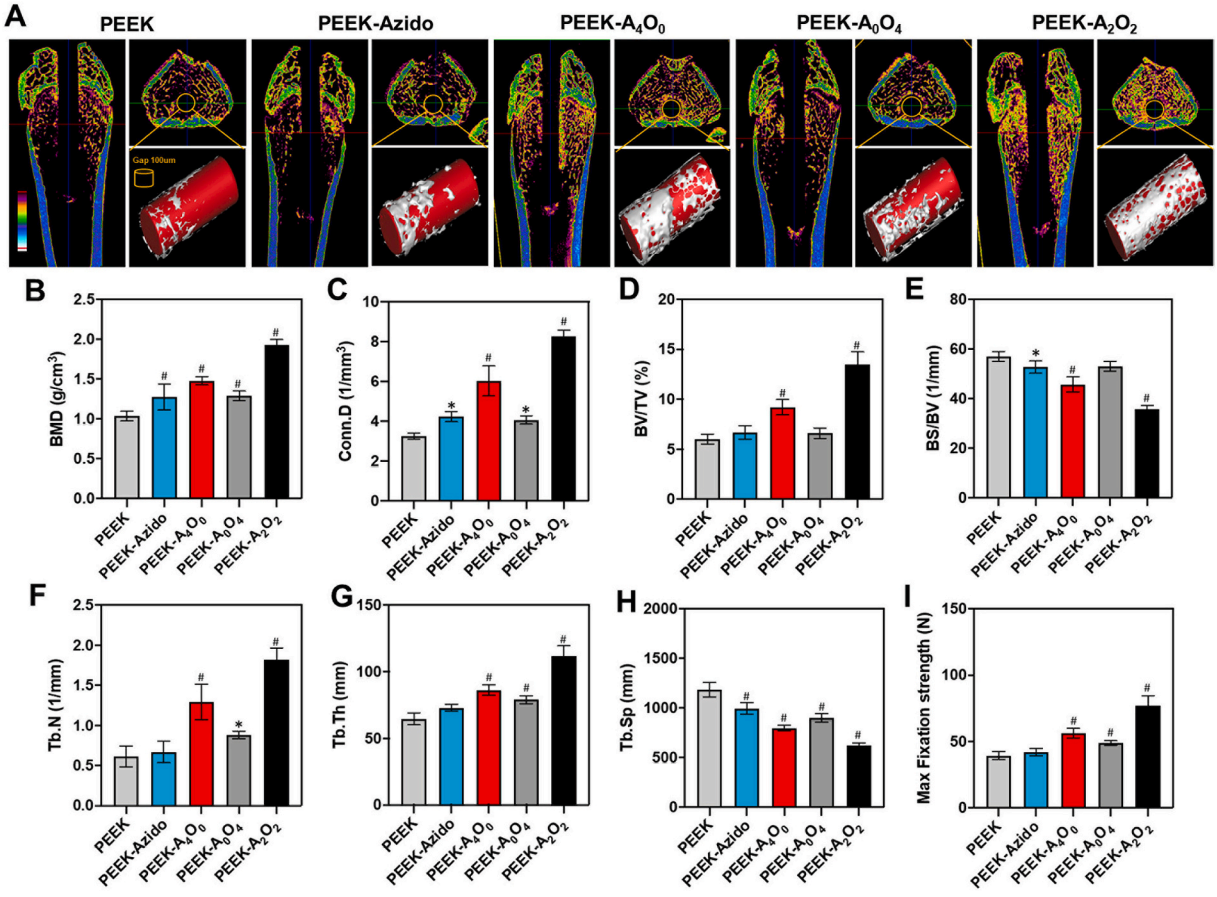

Fig. 9. In vivo peri-implant bone regeneration after 6 weeks of implantation. (A) Micro-CT scanning of the femurs containing different implants and the reconstructed 3D images. Corresponding to the bottom left colorful ruler, the cancellous bone is mainly yellow, the cortical bone is mainly blue, and the medullary cavity is black. (B–H) Quantitative analysis of BMD, Coon. D, BV/TV, BS/BV, Tb·Th and Tb. Sp (n = 6 per group). (I) Maximum interface fixation force in different groups determined by push-out testing (n = 4 per group). Statistically significant differences were indicated by *$p < 0.05$ and $^{\#}p < 0.01$ compared with the bare PEEK group.

4. Discussion

As an emerging kind of polymeric biomaterial for fabricating orthopedic and dental implants, PEEK possesses some superior characteristics including the well-matched mechanical properties, good biocompatibility and natural radiolucency [20,22,70]. However, the pristine PEEK material still suffers from the lack of anti-infectivity and osteo-inductivity, which severely hinders its clinical applications, as postoperative infection and aseptic loosening are the main reasons leading to the failure of orthopedic and dental implants [71]. Although various modification strategies have been proposed [21,23–25], the functionalizations of PEEK implants with anti-infectivity and osteo-inductivity are contradictory in most cases, because the active sites on sample surface are limited. Therefore, a right balance between the anti-infective and osteo-inductive functions is desirable for the implant material and pursued in the current study.

Herein, we reported a biomimetic surface strategy for rational integration and optimization of anti-infectivity and osteo-inductivity onto PEEK implants. In our design, a DOPA-rich peptide with clickable azido terminal is utilized to modify the implant surface initially, and then the introduced azido terminal can link to the DBCO group by bioorthogonal reaction, guaranteeing the subsequent grafting of anti-infective AMP and osteo-inductive OGP. Compared to the traditional strategy using osteogenic proteins for physical adsorption on the surface of PEEK implants [22,72], our strategy provides longer lasting effects because the physically attached proteins are prone to desorb from the implant surface and rapidly lose their activity in free state [73]. Furthermore, this strategy possesses numerous merits such as ease of operation, high efficiency and specificity, non-use of organic solvents as well as the uniform modification boding well the implants with irregular shapes. After two-step modification, the surface roughness and hydrophilicity of PEEK samples are both increased, which may contribute to the up-regulated cytocompatibility. What is more promising, the bioorthogonal clicking strategy allows precise collocation between AMP and OGP through changing their feeding molar ratios, and hence an optimal treatment of PEEK implants can be readily achieved in our study. By comprehensively considering the antibacterial and osteogenic performances *in vitro* and *in vivo*, the PEEK-A_2O_2 sample (with an AMP/OGP feeding ratio at 2:2) is superior to the other modified samples with regard to the satisfactory dual-effect of host defense and tissue repair.

In addition to the desirable bio-functions, the binding between the surface coating and PEEK substrates is another critical factor of success, as the functional coating should survive from the violence of surgical operations. In this regard, the as-prepared PEEK-A_2O_2 sample is compared to its counterpart implanted into the femoral of rat and taken out immediately. The analysis result of energy dispersive spectrometry (EDS) shows that the surface coating of PEEK-A_2O_2 sample can be well preserved after the multi-step operation of implantation and extraction (Fig. S7), which indicates the reliability of functional coating. To sum up, our surface bioengineering strategy combining mussel adhesion and bioorthogonal chemistry provides a versatile and feasible way to achieve multiple and durable bio-functions on biomaterials, thereby holds great promise in future applications.

5. Conclusions

In summary, here we developed an upgraded mussel-inspired surface strategy for multi-functionalization of PEEK osteoimplants by using a Mfps-mimic peptide with clickable azido terminal. The biomimetic peptide could adhere on PEEK surface and leave the azido groups for second-step bioorthogonal conjugations, thus enabling a facile surface integration of anti-infectivity and osteo-inductivity that are highly desired for osteoimplants. Specifically, a typical AMP (RWRWRW) and the active sequence of OGP (YGFGG) were co-clicked on PEEK osteoimplants. Rational changing the feeding molar ratios of AMP/OGP led to an optimal dual-functional coating on PEEK surfaces, which could defend against bacterial invasion and facilitate osteogenesis *in vivo*, and finally achieve bone-implant integration under infection condition. Overall, the combination of bioorthogonal chemistry and mussel adhesion mechanism can breed an improved mussel-like surface chemistry, which may be a promising solution for surface bioengineering of inert medical implants, in particular, for the rational integration of multiple biofunctions to match the clinic requirements.

CRediT authorship contribution statement

Meng Li: Methodology, Investigation, Data curation, Writing – original draft. **Jiaxiang Bai:** Methodology, Investigation, Data curation, Writing – original draft. **Huaqiang Tao:** Methodology, Investigation, Writing – original draft. **Li Hao:** Methodology, Investigation. **Weiling Yin:** Investigation. **Xiaoxue Ren:** Investigation. **Ang Gao:** Methodology, Investigation. **Ning Li:** Investigation. **Miao Wang:** Investigation, Validation. **Shiyuan Fang:** Investigation, Validation. **Yaozeng Xu:** Investigation, Writing – review & editing. **Liang Chen:** Investigation, Writing – review & editing. **Huilin Yang:** Investigation, Writing – review & editing. **Huaiyu Wang:** Conceptualization, Resources, Supervision, Writing – review & editing. **Guoqing Pan:** Conceptualization, Resources, Supervision, Writing – review & editing. **Dechun Geng:** Conceptualization, Resources, Supervision, Writing – review & editing.

Declaration of competing interest

The authors declare that they have no known competing financial interests or personal relationships that could have appeared to influence the work reported in this paper.

Acknowledgements

This work was supported by the National Key Research and Development Program of China (2019YFA0112000), Research and Development of Biomedical Materials and Substitution of Tissue and Organ Repair under the National Key R&D Program (2016YFC1101505), the National Natural Science Foundation of China (82072425, 82072498, 81873991, 81073990, 21875092, 31922040 and 81672238), the Young Medical Talents of Jiangsu Province (QNRC2016751), the Natural Science Foundation of Jiangsu Province (BK20180001), the Innovation and Entrepreneurship Program of Jiangsu Province, the “Six Talent Peaks” program of Jiangsu Province (2018-XCL-013), the Basic Applied Research Program of Suzhou City (SYS2018032, KJXW2017009), the Priority Academic Program Development of Jiangsu Higher Education Institutions (PAPD), and the Special Project of Diagnosis and Treatment for Clinical Diseases of Suzhou (LCZX202003).

Appendix A. Supplementary data

Supplementary data to this article can be found online at https://doi.org/10.1016/j.bioactmat.2021.07.002.

References

[1] P. Feng, P. Wu, C. Gao, Y. Yang, W. Guo, W. Yang, C. Shuai, A multimaterial scaffold with tunable properties: toward bone tissue repair, Adv. Sci. 5 (6) (2018), 1700817.
[2] W. Liu, J. Li, M. Cheng, Q. Wang, K.W.K. Yeung, P.K. Chu, X. Zhang, Zinc-modified sulfonated polyetheretherketone surface with immunomodulatory function for guiding cell fate and bone regeneration, Adv. Sci. 5 (10) (2018), 1800749.
[3] W. Liu, J. Li, M. Cheng, Q. Wang, Y. Qian, K.W.K. Yeung, P.K. Chu, X. Zhang, A surface-engineered polyetheretherketone biomaterial implant with direct and immunoregulatory antibacterial activity against methicillin-resistant Staphylococcus aureus, Biomaterials 208 (2019) 8–20.
[4] N.J. Shah, M.N. Hyder, J.S. Moskowitz, M.A. Quadir, S.W. Morton, H. J. Seeherman, R.F. Padera, M. Spector, P.T. Hammond, Surface-mediated bone tissue morphogenesis from tunable nanolayered implant coatings, Sci. Transl. Med. 5 (191) (2013), 191ra83.

[5] M.H. Malik, F. Jury, A. Bayat, W.E. Ollier, P.R. Kay, Genetic susceptibility to total hip arthroplasty failure: a preliminary study on the influence of matrix metalloproteinase 1, interleukin 6 polymorphisms and vitamin D receptor, Ann. Rheum. Dis. 66 (8) (2007) 1116–1120.

[6] L. Preller, G. Doekes, D. Heederik, R. Vermeulen, P.F. Vogelzang, J.S. Boleij, Disinfectant use as a risk factor for atopic sensitization and symptoms consistent with asthma: an epidemiological study, Eur. Respir. J. 9 (7) (1996) 1407–1413.

[7] X. Qu, H. Yang, B. Jia, Z. Yu, Y. Zheng, K. Dai, Biodegradable Zn-Cu alloys show antibacterial activity against MRSA bone infection by inhibiting pathogen adhesion and biofilm formation, Acta Biomater. 117 (2020) 400–417.

[8] F. Liu, X. Cheng, L. Xiao, Q. Wang, K. Yan, Z. Su, L. Wang, C. Ma, Y. Wang, Inside-outside Ag nanoparticles-loaded polylactic acid electrospun fiber for long-term antibacterial and bone regeneration, Int. J. Biol. Macromol. 167 (2021) 1338–1348.

[9] J. Pérez, F.J. Contreras-Moreno, F.J. Marcos-Torres, A. Moraleda-Muñoz, J. Muñoz-Dorado, The antibiotic crisis: how bacterial predators can help, Comput. Struct. Biotechnol. J. 18 (2020) 2547–2555.

[10] H. Hirakawa, J. Kurushima, Y. Hashimoto, H. Tomita, Progress overview of bacterial two-component regulatory systems as potential targets for antimicrobial chemotherapy, Antibiotics (Basel) 9 (10) (2020).

[11] A.R. Brochado, A. Telzerow, J. Bobonis, M. Banzhaf, A. Mateus, J. Selkrig, E. Huth, S. Bassler, J. Zamarreño Beas, M. Zietek, N. Ng, S. Foerster, B. Ezraty, B. Py, F. Barras, M.M. Savitski, P. Bork, S. Göttig, A. Typas, Species-specific activity of antibacterial drug combinations, Nature 559 (7713) (2018) 259–263.

[12] Y. Jiang, Y. Chen, Z. Song, Z. Tan, J. Cheng, Recent advances in design of antimicrobial peptides and polypeptides toward clinical translation, Adv. Drug Deliv. Rev. (2021).

[13] M. Wenzel, A.I. Chiriac, A. Otto, D. Zweytick, C. May, C. Schumacher, R. Gust, H. B. Albada, M. Penkova, U. Krämer, R. Erdmann, N. Metzler-Nolte, S.K. Straus, E. Bremer, D. Becher, H. Brötz-Oesterhelt, H.G. Sahl, J.E. Bandow, Small cationic antimicrobial peptides delocalize peripheral membrane proteins, Proc. Natl. Acad. Sci. U. S. A. 111 (14) (2014) E1409–E1418.

[14] M. Wenzel, P. Prochnow, C. Mowbray, C. Vuong, S. Höxtermann, J.J. Stepanek, H. B. Albada, J. Hall, N. Metzler-Nolte, J.E. Bandow, Towards profiles of resistance development and toxicity for the small cationic hexapeptide RWRWRW-NH2, Front Cell Dev Biol 4 (2016), 86.

[15] J. Chen, X. Shi, Y. Zhu, Y. Chen, M. Gao, H. Gao, L. Liu, L. Wang, C. Mao, Y. Wang, On-demand storage and release of antimicrobial peptides using Pandora's box-like nanotubes gated with a bacterial infection-responsive polymer, Theranostics 10 (1) (2020) 109–122.

[16] W. Tang, G.M. Policastro, G. Hua, K. Guo, J. Zhou, C. Wesdemiotis, G.L. Doll, M. L. Becker, Bioactive surface modification of metal oxides via catechol-bearing modular peptides: multivalent-binding, surface retention, and peptide bioactivity, J. Am. Chem. Soc. 136 (46) (2014) 16357–16367.

[17] Y. Qiao, X. Liu, X. Zhou, H. Zhang, W. Zhang, W. Xiao, G. Pan, W. Cui, H.A. Santos, Q. Shi, Gelatin templated polypeptide Co-Cross-Linked hydrogel for bone regeneration, Adv Healthc Mater 9 (1) (2020), e1901239.

[18] K.S. Stakleff, F. Lin, L.A. Smith Callahan, M.B. Wade, A. Esterle, J. Miller, M. Graham, M.L. Becker, Resorbable, amino acid-based poly(ester urea)s crosslinked with osteogenic growth peptide with enhanced mechanical properties and bioactivity, Acta Biomater. 9 (2) (2013) 5132–5142.

[19] J.L. Wang, J.K. Xu, C. Hopkins, D.H. Chow, L. Qin, Biodegradable magnesium-based implants in orthopedics-A general review and perspectives, Adv. Sci. 7 (8) (2020), 1902443.

[20] X. Meng, J. Zhang, J. Chen, B. Nie, B. Yue, W. Zhang, Z. Lyu, T. Long, Y. Wang, KR-12 coating of polyetheretherketone (PEEK) surface via polydopamine improves osteointegration and antibacterial activity in vivo, J. Mater. Chem. B 8 (44) (2020) 10190–10204.

[21] M. Yakufu, Z. Wang, Y. Wang, Z. Jiao, M. Guo, J. Liu, P. Zhang, Covalently functionalized poly (etheretherketone) implants with osteogenic growth peptide (OGP) to improve osteogenesis activity, RSC Adv. 10 (17) (2020) 9777–9785.

[22] X. Yuan, L. Ouyang, Y. Luo, Z. Sun, C. Yang, J. Wang, X. Liu, X. Zhang, Multifunctional sulfonated polyetheretherketone coating with beta-defensin-14 for yielding durable and broad-spectrum antibacterial activity and osseointegration, Acta Biomater. 86 (2019) 323–337.

[23] Y. Zhao, H.M. Wong, S.C. Lui, E.Y. Chong, G. Wu, X. Zhao, C. Wang, H. Pan, K. M. Cheung, S. Wu, P.K. Chu, K.W. Yeung, Plasma surface functionalized polyetheretherketone for enhanced osseo-integration at bone-implant interface, ACS Appl. Mater. Interfaces 8 (6) (2016) 3901–3911.

[24] A. Gao, Q. Liao, L. Xie, G. Wang, W. Zhang, Y. Wu, P. Li, M. Guan, H. Pan, L. Tong, P.K. Chu, H. Wang, Tuning the surface immunomodulatory functions of polyetheretherketone for enhanced osseointegration, Biomaterials 230 (2020), 119642.

[25] Y. Zhao, H.M. Wong, W. Wang, P. Li, Z. Xu, E.Y. Chong, C.H. Yan, K.W. Yeung, P. K. Chu, Cytocompatibility, osseointegration, and bioactivity of three-dimensional porous and nanostructured network on polyetheretherketone, Biomaterials 34 (37) (2013) 9264–9277.

[26] T. Wan, Z. Jiao, M. Guo, Z. Wang, Y. Wan, K. Lin, Q. Liu, P. Zhang, Gaseous sulfur trioxide induced controllable sulfonation promoting biomineralization and osseointegration of polyetheretherketone implants, Bioactive Materials 5 (4) (2020) 1004–1017.

[27] L. Ouyang, Y. Zhao, G. Jin, T. Lu, J. Li, Y. Qiao, C. Ning, X. Zhang, P.K. Chu, X. Liu, Influence of sulfur content on bone formation and antibacterial ability of sulfonated PEEK, Biomaterials 83 (2016) 115–126.

[28] C. Zhang, B. Wu, Y. Zhou, F. Zhou, W. Liu, Z. Wang, Mussel-inspired hydrogels: from design principles to promising applications, Chem. Soc. Rev. 49 (11) (2020) 3605–3637.

[29] Y. Jing, Q. Xia, X. Liu, Y. Wang, Production of low-freezing-point highly branched alkanes through Michael addition, ChemSusChem 10 (24) (2017) 4817–4823.

[30] Y. Sang, Y. Cao, L. Wang, W. Yan, T. Chen, J. Huang, Y.N. Liu, N-rich porous organic polymers based on Schiff base reaction for CO(2) capture and mercury(II) adsorption, J. Colloid Interface Sci. 587 (2020) 121–130.

[31] M. Liu, G. Zeng, K. Wang, Q. Wan, L. Tao, X. Zhang, Y. Wei, Recent developments in polydopamine: an emerging soft matter for surface modification and biomedical applications, Nanoscale 8 (38) (2016) 16819–16840.

[32] Z. Yang, X. Zhao, R. Hao, Q. Tu, X. Tian, Y. Xiao, K. Xiong, M. Wang, Y. Feng, N. Huang, G. Pan, Bioclickable and mussel adhesive peptide mimics for engineering vascular stent surfaces, Proc. Natl. Acad. Sci. U. S. A. 117 (28) (2020) 16127–16137.

[33] M. Czuban, M.W. Kulka, L. Wang, A. Koliszak, K. Achazi, C. Schlaich, I.S. Donskyi, M. Di Luca, J.M. Mejia Oneto, M. Royzen, R. Haag, A. Trampuz, Titanium coating with mussel inspired polymer and bio-orthogonal chemistry enhances antimicrobial activity against Staphylococcus aureus, Mater Sci Eng C Mater Biol Appl 116 (2020), 111109.

[34] S. Das, N.R. Martinez Rodriguez, W. Wei, J.H. Waite, J.N. Israelachvili, Peptide length and dopa determine iron-mediated cohesion of mussel foot proteins, Adv. Funct. Mater. 25 (36) (2015) 5840–5847.

[35] R. Sasmal, N. Das Saha, M. Pahwa, S. Rao, D. Joshi, M.S. Inamdar, V. Sheeba, S. S. Agasti, Synthetic host-guest assembly in cells and tissues: fast, stable, and selective bioorthogonal imaging via molecular recognition, Anal. Chem. 90 (19) (2018) 11305–11314.

[36] G. Pan, S. Sun, W. Zhang, R. Zhao, W. Cui, F. He, L. Huang, S.-H. Lee, K.J. Shea, Q. Shi, H. Yang, Biomimetic design of mussel-derived bioactive peptides for dual-functionalization of titanium-based biomaterials, J. Am. Chem. Soc. 138 (45) (2016) 15078–15086.

[37] J. Bai, H. Wang, H. Chen, G. Ge, M. Wang, A. Gao, L. Tong, Y. Xu, H. Yang, G. Pan, P.K. Chu, D. Geng, Biomimetic osteogenic peptide with mussel adhesion and osteoimmunomodulatory functions to ameliorate interfacial osseointegration under chronic inflammation, Biomaterials 255 (2020), 120197.

[38] X. Tian, X. Chen, Y. Feng, Y. Duan, M. Dong, G. Pan, L. Liu, Biomimetic fabrication of dynamic biointerfaces with optional and diversified bioactivities through reversible covalent and bioorthogonal chemistry, Chem. Eng. J. 398 (2020), 125620.

[39] S. Seo, D.W. Lee, J.S. Ahn, K. Cunha, E. Filippidi, S.W. Ju, E. Shin, B.S. Kim, Z. A. Levine, R.D. Lins, J.N. Israelachvili, J.H. Waite, M.T. Valentine, J.E. Shea, B. K. Ahn, Significant performance enhancement of polymer resins by bioinspired dynamic bonding, Adv. Mater. 29 (39) (2017).

[40] S. Ribeiro, E. Radvar, Y. Shi, J. Borges, R.P. Pirraco, I.B. Leonor, J.F. Mano, R. L. Reis, Á. Mata, H.S. Azevedo, Nanostructured interfacial self-assembled peptide-polymer membranes for enhanced mineralization and cell adhesion, Nanoscale 9 (36) (2017) 13670–13682.

[41] S.C. Chen, K.T. Chen, A.F. Jou, Polydopamine-gold composite-based electrochemical biosensor using dual-amplification strategy for detecting pancreatic cancer-associated microRNA, Biosens. Bioelectron. 173 (2021), 112815.

[42] A. Martens, P. Weis, M.C. Krummer, M. Kreuzer, A. Meierhöfer, S.C. Meier, J. Bohnenberger, H. Scherer, I. Riddlestone, I. Krossing, Facile and systematic access to the least-coordinating WCA [(R(F)O)(3)Al-F-Al(OR(F))(3)](-) and its more Lewis-basic brother [F-Al(OR(F))(3)](-) (R(F) = C(CF(3))(3)), Chem. Sci. 9 (35) (2018) 7058–7068.

[43] J. Zhang, E. Wehrle, P. Adamek, G.R. Paul, X.H. Qin, M. Rubert, R. Müller, Optimization of mechanical stiffness and cell density of 3D bioprinted cell-laden scaffolds improves extracellular matrix mineralization and cellular organization for bone tissue engineering, Acta Biomater. 114 (2020) 307–322.

[44] M. Li, A. Zhang, J. Li, J. Zhou, Y. Zheng, C. Zhang, D. Xia, H. Mao, J. Zhao, Osteoblast/fibroblast coculture derived bioactive ECM with unique matrisome profile facilitates bone regeneration, Bioact Mater 5 (4) (2020) 938–948.

[45] X. Li, Q. Zou, Y. Man, W. Li, Synergistic effects of novel superparamagnetic/upconversion HA material and Ti/magnet implant on biological performance and long-term in vivo tracking, Small 15 (31) (2019), e1901617.

[46] B.W. Park, S.H. Jung, S. Das, S.M. Lee, J.H. Park, H. Kim, J.W. Hwang, S. Lee, H. J. Kim, H.Y. Kim, S. Jung, D.W. Cho, J. Jang, K. Ban, H.J. Park, Vivo priming of human mesenchymal stem cells with hepatocyte growth factor-engineered mesenchymal stem cells promotes therapeutic potential for cardiac repair, Sci Adv 6 (13) (2020), eaay6994.

[47] J.B. Green, S. Bickner, P.W. Carter, T. Fulghum, M. Luebke, M.A. Nordhaus, S. Strathmann, Antimicrobial testing for surface-immobilized agents with a surface-separated live-dead staining method, Biotechnol. Bioeng. 108 (1) (2011) 231–236.

[48] G. Wang, L. Zheng, H. Zhao, J. Miao, C. Sun, H. Liu, Z. Huang, X. Yu, J. Wang, X. Tao, Construction of a fluorescent nanostructured chitosan-hydroxyapatite scaffold by nanocrystallon induced biomimetic mineralization and its cell biocompatibility, ACS Appl. Mater. Interfaces 3 (5) (2011) 1692–1701.

[49] S. Atefyekta, M. Pihl, C. Lindsay, S.C. Heilshorn, M. Andersson, Antibiofilm elastin-like polypeptide coatings: functionality, stability, and selectivity, Acta Biomater. 83 (2019) 245–256.

[50] N.B. da Cunha, N.B. Cobacho, J.F.C. Viana, L.A. Lima, K.B.O. Sampaio, S.S. M. Dohms, A.C.R. Ferreira, C. de la Fuente-Núñez, F.F. Costa, O.L. Franco, S. C. Dias, The next generation of antimicrobial peptides (AMPs) as molecular therapeutic tools for the treatment of diseases with social and economic impacts, Drug Discov. Today 22 (2) (2017) 234–248.

[51] S. Beckerdite, C. Mooney, J. Weiss, R. Franson, P. Elsbach, Early and discrete changes in permeability of Escherichia coli and certain other gram-negative bacteria during killing by granulocytes, J. Exp. Med. 140 (2) (1974) 396–409.
[52] N. Batra, J. Singh, A. Joshi, S. Bhatia, Applications of β-gal-III isozyme from Bacillus coagulans RCS3, in lactose hydrolysis, Int. J. Biol. Macromol. 49 (5) (2011) 879–884.
[53] E. Ulukaya, F. Ozdikicioglu, A.Y. Oral, M. Demirci, The MTT assay yields a relatively lower result of growth inhibition than the ATP assay depending on the chemotherapeutic drugs tested, Toxicol. Vitro 22 (1) (2008) 232–239.
[54] H. Pereira, I.F. Cengiz, F.R. Maia, F. Bartolomeu, J.M. Oliveira, R.L. Reis, F.S. Silva, Physicochemical properties and cytocompatibility assessment of non-degradable scaffolds for bone tissue engineering applications, J Mech Behav Biomed Mater 112 (2020), 103997.
[55] A.K. Teotia, K. Dienel, I. Qayoom, B. van Bochove, S. Gupta, J. Partanen, J. Seppälä, A. Kumar, Improved bone regeneration in rabbit bone defects using 3D printed composite scaffolds functionalized with osteoinductive factors, ACS Appl. Mater. Interfaces (2020).
[56] L. Osman, A.H. Chester, P. Sarathchandra, N. Latif, W. Meng, P.M. Taylor, M. H. Yacoub, A novel role of the sympatho-adrenergic system in regulating valve calcification, Circulation 116 (11 Suppl) (2007) I282–I287.
[57] Y. Ikebuchi, S. Aoki, M. Honma, M. Hayashi, Y. Sugamori, M. Khan, Y. Kariya, G. Kato, Y. Tabata, J.M. Penninger, N. Udagawa, K. Aoki, H. Suzuki, Coupling of bone resorption and formation by RANKL reverse signalling, Nature 561 (7722) (2018) 195–200.
[58] J. Lee, S. Lee, T. Ahmad, S.K. Madhurakkat Perikamana, J. Lee, E.M. Kim, H. Shin, Human adipose-derived stem cell spheroids incorporating platelet-derived growth factor (PDGF) and bio-minerals for vascularized bone tissue engineering, Biomaterials 255 (2020), 120192.
[59] R.R. McCarthy, M.W. Ullah, P. Booth, E. Pei, G. Yang, The use of bacterial polysaccharides in bioprinting, Biotechnol. Adv. 37 (8) (2019), 107448.
[60] M.F.P. Graça, D. de Melo-Diogo, I.J. Correia, A.F. Moreira, Electrospun asymmetric membranes as promising wound dressings: a review, Pharmaceutics 13 (2) (2021).
[61] S. Fahimirad, H. Abtahi, P. Satei, E. Ghaznavi-Rad, M. Moslehi, A. Ganji, Wound healing performance of PCL/chitosan based electrospun nanofiber electrosprayed with curcumin loaded chitosan nanoparticles, Carbohydr. Polym. 259 (2021), 117640.
[62] H.T. Green, M.A. O'Donoghue, M.D. Shaw, C. Dowling, Penetration of ceftazidime into intracranial abscess, J. Antimicrob. Chemother. 24 (3) (1989) 431–436.
[63] J.L. Goodman, C. Nelson, B. Vitale, J.E. Madigan, J.S. Dumler, T.J. Kurtti, U. G. Munderloh, Direct cultivation of the causative agent of human granulocytic ehrlichiosis, N. Engl. J. Med. 334 (4) (1996) 209–215.
[64] Q. Ji, Z. Wang, Z. Jiao, Y. Wang, Z. Wu, P. Wang, Y. Zhu, S. Sun, Y. Liu, P. Zhang, Biomimetic polyetheretherketone microcarriers with specific surface topography and self-secreted extracellular matrix for large-scale cell expansion, Regen Biomater 7 (1) (2020) 109–118.
[65] J. Knaus, D. Schaffarczyk, H. Cölfen, On the future design of bio-inspired polyetheretherketone dental implants, Macromol. Biosci. 20 (1) (2020), e1900239.
[66] W.C. O'Neill, K.A. Lomashvili, H.H. Malluche, M.C. Faugere, B.L. Riser, Treatment with pyrophosphate inhibits uremic vascular calcification, Kidney Int. 79 (5) (2011) 512–517.
[67] H. Liu, Z. Liu, J. Du, J. He, P. Lin, B. Amini, M.W. Starbuck, N. Novane, J.J. Shah, R.E. Davis, J. Hou, R.F. Gagel, J. Yang, Thymidine phosphorylase exerts complex effects on bone resorption and formation in myeloma, Sci. Transl. Med. 8 (353) (2016), 353ra113.
[68] R.C. Pereira, D.S. Bischoff, D. Yamaguchi, I.B. Salusky, K. Wesseling-Perry, Micro-CT in the assessment of pediatric renal osteodystrophy by bone histomorphometry, Clin. J. Am. Soc. Nephrol. 11 (3) (2016) 481–487.
[69] Y. Yu, G. Jin, Y. Xue, D. Wang, X. Liu, J. Sun, Multifunctions of dual Zn/Mg ion co-implanted titanium on osteogenesis, angiogenesis and bacteria inhibition for dental implants, Acta Biomater. 49 (2017) 590–603.
[70] S.M. Kurtz, J.N. Devine, PEEK biomaterials in trauma, orthopedic, and spinal implants, Biomaterials 28 (32) (2007) 4845–4869.
[71] M. Montalti, B. Bordini, S. Natali, M. Cosentino, F. Castagnini, F. Traina, Revisions for periprosthetic hip infections do not fail more than revisions for aseptic loosening, but mortality is higher, J. Arthroplasty 36 (3) (2021) 1074–1079.
[72] J. Wu, L. Li, C. Fu, F. Yang, Z. Jiao, X. Shi, Y. Ito, Z. Wang, Q. Liu, P. Zhang, Micro-porous polyetheretherketone implants decorated with BMP-2 via phosphorylated gelatin coating for enhancing cell adhesion and osteogenic differentiation, Colloids Surf. B Biointerfaces 169 (2018) 233–241.
[73] Z. Sun, L. Ouyang, X. Ma, Y. Qiao, X. Liu, Controllable and durable release of BMP-2-loaded 3D porous sulfonated polyetheretherketone (PEEK) for osteogenic activity enhancement, Colloids Surf. B Biointerfaces 171 (2018) 668–674.